

# SoDaCam: Software-defined Cameras via Single-Photon Imaging

Varun Sundar<sup>†</sup>

vsundar4@cs.wisc.edu

Andrei Ardelean<sup>‡</sup>

a.ardelean@epfl.ch

Tristan Swedish<sup>§</sup>

tristan@ubicept.com

Claudio Bruschini<sup>‡</sup>

{claudio.bruschini, edoardo.charbon}@epfl.ch

Edoardo Charbon<sup>‡</sup>

Mohit Gupta<sup>†,§</sup>

mohitg@cs.wisc.edu

<sup>†</sup>University of Wisconsin-Madison    <sup>‡</sup>École polytechnique fédérale de Lausanne    <sup>§</sup>Ubicept

## Abstract

*Reinterpretable cameras are defined by their post-processing capabilities that exceed traditional imaging. We present “SoDaCam” that provides reinterpretable cameras at the granularity of photons, from photon-cubes acquired by single-photon devices. Photon-cubes represent the spatio-temporal detections of photons as a sequence of binary frames, at frame-rates as high as 100 kHz. We show that simple transformations of the photon-cube, or photon-cube projections, provide the functionality of numerous imaging systems including: exposure bracketing, flutter shutter cameras, video compressive systems, event cameras, and even cameras that move during exposure. Our photon-cube projections offer the flexibility of being software-defined constructs that are only limited by what is computable, and shot-noise. We exploit this flexibility to provide new capabilities for the emulated cameras. As an added benefit, our projections provide camera-dependent compression of photon-cubes, which we demonstrate using an implementation of our projections on a novel compute architecture that is designed for single-photon imaging.*

## 1. Introduction

Throughout the history of imaging, sensing technologies and the corresponding processing have developed hand-in-hand. In fact, sensing technologies have, to some extent, defined the scope of processing captured data. In the film era, instances of such processing included dodging and burning. The advent of digital cameras provided processing at the granularity of pixels and paved the way for modern computer vision. Light field cameras [34, 78], by sampling the plenoptic function [2], allowed post-capture processing at

the granularity of light rays, enabling novel functionalities such as refocusing photos after-capture. The logical limit of post-capture processing, given the fundamental quantization of light, would be at the level of individual photons. What would imaging look like if we could perform computational processing on individual photons?

In this work, we show that photon data captured by a new class of single-photon detectors, called single-photon avalanche diodes (SPADs), makes it possible to emulate a wide range of imaging modalities such as exposure bracketing [12], video compressive systems [38, 55] and event cameras [52, 60]. A user then has the flexibility to choose one (or even multiple) of these functionalities *post-capture* (Fig. 1 (top)). SPAD arrays can operate as extremely high frame-rate photon detectors (~100 kHz), producing a temporal sequence of binary frames called a photon-cube [16]. We show that computing *photon-cube projections*, which are simple linear and shift operations, can reinterpret the photon-cube to achieve novel post-capture imaging functionalities in a software-defined manner (Fig. 1 (middle)).

As case studies, we emulate three distinct imagers: high-speed video compressive imaging; event cameras which respond to dynamic scene content; and motion projections which emulate sensor motion, without any real camera movement. Fig. 1 (bottom) shows the outputs of these cameras that are derived from the same photon-cube.

**Computing photon-cube projections.** One way to obtain photon-cube projections is to read the entire photon-cube off the SPAD array and then perform relevant computations off-chip; we adopt this strategy for our experiments in Secs. 6.1 and 6.2. While reasonable for certain applications, reading out photon-cubes requires an exorbitant data bandwidth, which can be up to 100 Gbps for a 1 MPixel array—well beyond the capacity of existing data peripherals. Such readout considerations will become center stage as large-format SPAD arrays are fabricated [48, 49].

An alternative is to avoid transferring the entire photon-

\*Corresponding author: Varun Sundar. This research was supported in parts by NSF CAREER award 1943149, NSF award CNS-2107060, and the Swiss National Science Foundation grant 200021\_166289. We also thank Paul Mos for providing access to SwissSPAD2 acquisition software.

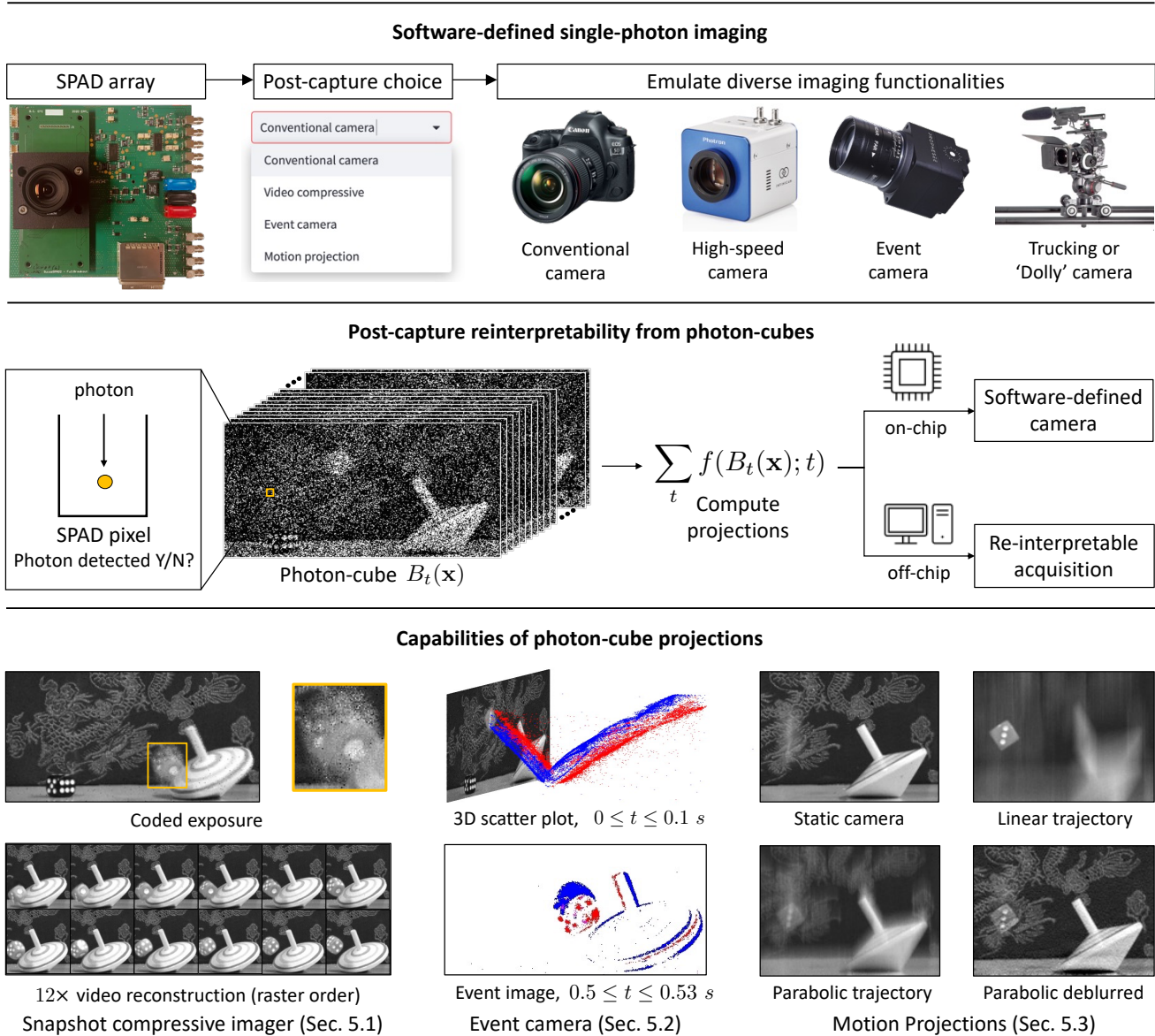


Figure 1: (*top*) **SoDaCam** can emulate a variety of cameras from the photon-cubes acquired by single-photon devices. (*middle*) Photon-cubes represent the spatio-temporal detection of photons as a sequence of binary frames. Projections of the photon-cube, when computed either on or off-chip, result in reinterpretible and software-defined cameras. We demonstrate the versatility of photon-cube projections on a **real dynamic scene**: a die falls on a table, bounces, spins in the air, and later ricochets off a nearby toy top. (*bottom*) The cameras emulated by our photon-cube projections can produce a  $12\times$  high-speed video from a single compressive snapshot, event-stream representations of two time intervals (blue and red depict positive and negative spikes respectively), an image where the die appears stationary, as well as a motion-deblurred image.

cube by computing projections near sensor. As a proof-of-concept, we implement photon-cube projections on UltraPhase [1], a recently-developed programmable SPAD imager with independent processing cores that have dedicated RAM and instruction memory. We show, in Sec. 6.3, that computing projections on-chip greatly reduces sensor read-out and, as a consequence, power consumption.

**Implications: Toward a photon-level software-defined camera.** The photon-cube projections introduced in this paper are computational constructs that provide a realization of *software-defined cameras* or *SoDaCam*. Being software-defined, SoDaCam can emulate multiple cameras simultaneously without additional hardware complexity. SoDaCam, by going beyond baked-in hardware choices,

unlocks hitherto unseen capabilities—such as 2000 FPS video from 25 Hz readout (Fig. 7); event imaging in very low-light conditions (Fig. 9); and motion stacks, which are a stack of images wherein each image, objects only in certain velocity ranges appear sharp (Fig. 6).

**Limitations.** The SPAD array [19] used in this work has a relatively low spatial resolution ( $512 \times 256$ ), and a low fill-factor ( $\sim 10\%$ ) owing to the lack of microlenses in the prototype used. Similarly, the near-sensor processor that we use has limited capabilities compared to off-chip processors. However, with rapid progress in the development of single-photon cameras [48, 49] and increasing interest in near-sensor processors, we anticipate that many of these shortcomings will be addressed in the upcoming years.

## 2. Related Work

**Reinterpretable imaging** has previously been explored at the granularity of light rays [3], by modulating the plenoptic function, and at the level of spatio-temporal voxels [20], by using fast per-pixel shutters. SoDaCam represents a logical culmination of reinterpretable at the level of photon detections, that facilitates multiple post-capture imaging functionalities.

**Programmable imaging** using a digital micromirror device was first introduced in Nayar et al. [51] to perform *pre-capture* radiometric manipulations. Modern programmable cameras are typically near-sensor processors [8, 69, 71] that can perform limited operations in analog [46, 55, 69], while more complex operations [9, 45] occur after analog-to-digital conversion (ADC). In contrast, by performing *post-capture* computations directly on photon detections, we can perform complex operations without incurring the read-noise penalty that is associated with ADC.

**Passive single-photon imaging.** Only recently have SPADs been utilized as passive imaging devices, with applications in high-dynamic range imaging [29, 30, 37, 50], motion-compensation [31, 58], burst photography [11, 42] and object tracking [22]. Compared to compute-intensive burst-photography methods [11], our proposed techniques involve lightweight computations that can be performed near sensor. These computations can also be performed using other single-photon imagers such as Jots [15, 17], which feature higher sensor resolution and photon-efficiency [40], albeit at lower frame-rates and higher read noise.

**Reducing the readout of SPADs.** Several data reduction strategies have been proposed in the context of SPADs that are used to timestamp incident photons, including: coarse histograms [13, 23, 56], compressive histograms [21], and

measuring differential time-of-arrivals [70, 77]. When SPADs are operated as photon-detectors, multi-bit counting [48], or summing binary frames, can reduce readout. While compression is not our main objective, we show that photon-cube projections act as camera-specific compression schemes that dramatically reduce sensor readout.

## 3. Background: Single-Photon Imaging Model

A SPAD array captures incident light as a *photon-cube*: a temporal sequence of binary frames that represents the pixel-wise detection of photons across their respective exposure windows. We can model the stochastic arrival of photons as a Poisson process [72], allowing us to treat spatio-temporal values of the photon-cube as independent Bernoulli random variables with

$$\Pr\{B_t(\mathbf{x}) = 1\} = 1 - e^{-(\eta\Phi(\mathbf{x},t)+r_q)w_{\text{exp}}}, \quad (1)$$

where  $B_t(\mathbf{x})$  represents the value of the photon-cube at pixel  $\mathbf{x}$  and exposure index  $1 \leq t \leq T$ , which receives a mean incident flux of intensity  $\Phi(\mathbf{x}, t)$  across its exposure of duration  $w_{\text{exp}}$ . Additionally,  $\eta$  is the photon detection efficiency of the SPAD, and  $r_q$  denotes the sensor’s dark count rate—which is the rate of spurious counts unrelated to incident photons. While individual binary frames are extremely noisy, the temporal sum of the photon-cube

$$\mathcal{I}_{\text{sum}}(\mathbf{x}) := \sum_{t=1}^T B_t(\mathbf{x}), \quad (2)$$

can produce an ‘image’ of the scene that is sharp in static regions, but blurry in dynamic regions (Fig. 2 (top)). Indeed, in static regions, the sum-image can be used to derive a maximum likelihood estimator of the scene intensity [4], given by  $\hat{\Phi}(\mathbf{x}) = -\ln(1 - T^{-1}\mathcal{I}_{\text{sum}}(\mathbf{x}))/\eta w_{\text{exp}} - r_q/w_{\text{exp}}$ .

## 4. Projections of the Photon-Cube

The temporal sum described in Eq. (2) is a simple instance of projections of a photon-cube. Our key observation is that it is possible to compute a wide range of photon-cube projections, each of which emulates a unique sensing modality *post-capture*—including modalities that are difficult to achieve with conventional cameras. For example, varying the number of bit-planes that are summed over emulates exposure bracketing [12, 43], which is typically used for HDR imaging. Compared to conventional exposure bracketing, the emulated exposure stack, being software-defined, does not require spatial and temporal registration, which can often be error-prone. Fig. 2 (top) shows an example of an exposure stack computed from a photon-cube.

Going further, we can gradually increase the complexity of the projections. For example, consider a *coded exposure*

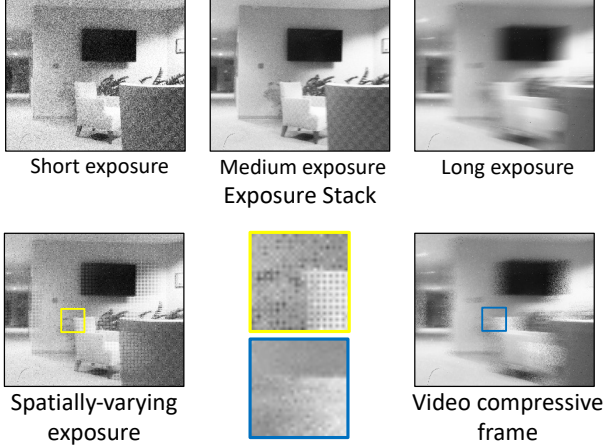


Figure 2: **Coded exposures from photon-cubes.** (top) An exposure stack with sum-images computed using 250, 500, and 1000 bit-planes. Short exposures are noisy while long exposures exhibit motion blur. (bottom) Spatially-varying exposure that uses a quad pattern [32] (see inset), and a video compressive frame that uses 16 random binary masks to modulate the photon-cube. Zoom-in to see details.

projection that multiplexes bit-planes with a temporal code

$$\mathcal{I}_{\text{flutter}}(\mathbf{x}) := \sum_{t=1}^T C_t B_t(\mathbf{x}), \quad (3)$$

where  $C_t$  is the temporal code. An example of globally-coded exposures is the flutter shutter camera [53], which uses pseudo-random binary codes for motion-deblurring.

More general coded exposures can be obtained via spatially-varying temporal coding patterns  $C_t(\mathbf{x})$ :

$$\mathcal{I}_{\text{coded}}(\mathbf{x}) := \sum_{t=1}^T C_t(\mathbf{x}) B_t(\mathbf{x}). \quad (4)$$

Fig. 2 (bottom) shows spatially-varying exposures that use a quad (Bayer-like) spatial pattern and random binary masks. With photon-cubes, we can perform spatially-varying coding without bulky spatial light modulators, similar to focal-plane sensor-processors [46, 69]. Moreover, we can capture multiple coded exposures simultaneously, which is challenging to realize in existing sensors. In Sec. 5.1, we describe coding patterns for video compressive sensing.

Spatial and temporal gradients form the building blocks of several computer vision algorithms [7, 11, 24, 26, 39]. Given this, another projection of interest is temporal contrast, i.e., a derivative filter preceded by a smoothing filter:

$$\mathcal{I}_{\text{contrast}}(\mathbf{x}, t) := D_t \circ G * B_t(\mathbf{x}), \quad (5)$$

where  $D_t$  is the difference operator,  $G$  could be exponential or Gaussian smoothing,  $\circ$  denotes function composition,

and  $*$  denotes convolution. Due to their sparse nature, gradients form the basis of bandwidth- and power-efficient event cameras [6, 14, 36, 60], which we emulate in Sec. 5.2.

So far, we have considered projections taken only along the time axis. Next, we consider a more general class of *spatio-temporal projections* that lead to novel functionalities. For instance, computing a simple projection, such as the temporal sum, along arbitrary spatio-temporal directions emulates sensor motion during exposure time [33], but *without moving the sensor*. We achieve this by shifting bit-planes and computing their sum:

$$\mathcal{I}_{\text{shift}}(\mathbf{x}) := \sum_{t=1}^T B_t(\mathbf{x} + \mathbf{r}(t)), \quad (6)$$

where  $\mathbf{r}$  is a discretized 2D trajectory that determines sensor motion. Outside a software-defined framework, such projections are hard to realize without physical actuators. We describe the capabilities of *motion projections* in Sec. 5.3.

In summary, the proposed photon-cube projections are simple linear and shift operators that lead to a diverse set of post-capture imaging functionalities. These projections pave the way for future ‘swiss-army-knife’ imaging systems that achieve *multiple functionalities* (e.g., *event cameras, high-speed cameras, conventional cameras, HDR cameras*) *simultaneously with a single sensor*. Finally, these projections can be computed efficiently in an online manner, which makes on-chip implementation viable (Sec. 6.3).

At this point, we note that a key enabling factor of photon-cube projections is the extremely high temporal-sampling rate of SPADs. Indeed, the temporal sampling rate determines key aspects of sensor emulation, such as the discretization of temporal derivatives and motion trajectories. This raises a natural question: can we use conventional high-speed cameras for computing projections?

**Trade-off between frame-rate and SNR.** In principle, photon-cube projections can be computed using regular (CMOS or CCD based) high-speed cameras. Unfortunately, each frame captured by a high-speed camera incurs a read-noise penalty, which increases with the camera’s frame-rate [6]. In fact, the read noise levels of high-speed cameras [1] can be 10–30× higher than consumer cameras [28]. Coupled with the low per-frame incident flux at high frame-rates, high levels of read noise result in extremely low SNRs. In contrast, SPADs do not incur a per-frame read noise and are limited only by the fundamental photon noise. Hence, for the post-capture software-defined functionalities proposed here, it is imperative to use SPADs.

## 5. Emulating Cameras from Photon-Cubes

Sec. 4 presented the concept of photon-cube projections and its potential for achieving multiple post-capture imag-

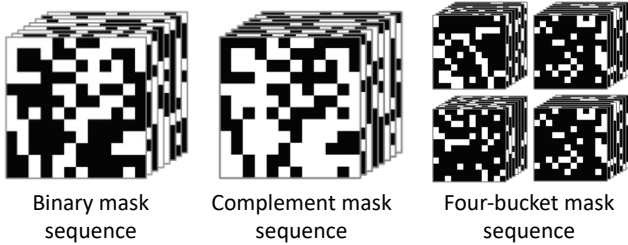


Figure 3: **Modulating masks for video compressive sensing.** (left) A single VCS measurement temporally compresses a sequence of frames using binary random masks. (center) Two-bucket cameras capture an additional measurement by using the complementary mask sequence. (right) We propose using multi-bucket captures by randomly choosing an active bucket for each frame. Both two-bucket and multi-bucket captures have 100% light efficiency. All masks are visualized here for  $16 \times 16$  pixels.

ing functionalities. As case studies, we now demonstrate three imaging modalities: video compressive sensing, event cameras, and motion-projection cameras. These modalities have been well-studied over several years; in particular, there exist active research communities around video compressive sensing and event cameras today. We also show new variants of these imaging systems that arise from the software-defined nature of photon-cube projections.

### 5.1. Video Compressive Sensing

Video compressive systems *optically* multiplex light with random binary masks, such as the patterns in Fig. 3 (left). As discussed in the previous section, such multiplexing can be achieved *computationally* using photon-cubes.

**Two-bucket cameras.** One drawback of capturing coded measurements is the light loss due to blocking of incident light. To prevent loss of light, coded two-bucket cameras [69] capture an additional measurement that is modulated by the complementary mask sequence (Fig. 3 (center)). Such measurements recover higher quality frames, even after accounting for the extra readout [9, 14]. Two-bucket captures can be readily derived from photon-cubes, by implementing Eq. (4) with the additional mask sequence.

**Multi-bucket cameras.** We can extend the idea of two-bucket captures to multi-bucket captures by accumulating bit-planes in one of  $k$  buckets that is randomly chosen at each time instant and pixel location. Since multiplexing is performed computationally, we do not face any loss in photoreceptive area that [59, 68] hampers existing multi-bucket sensors. Multi-bucket captures can reconstruct a large number of frames by better conditioning video recovery and

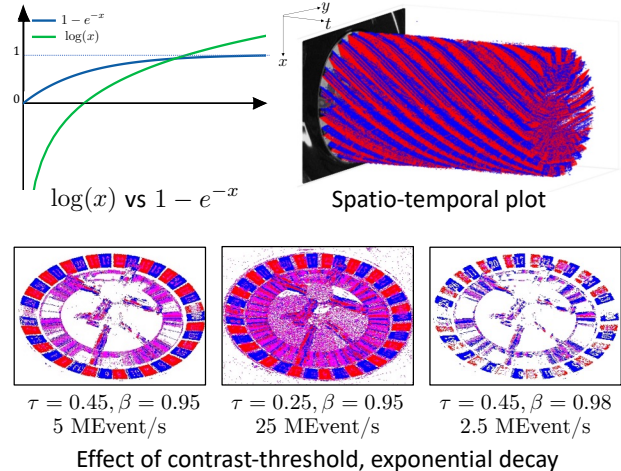


Figure 4: **Event stream from photon-cubes.** (top left) By exploiting the non-linear response curve of SPADs to encode brightness, we can avoid the underflow issues of a log-response. We visualize events generated from photon-cubes using a 3D scatter plot of polarities (top right, 14000 bit-planes), and frame accumulation of events (bottom, 1200 bit-planes). Blue and red denote positive and negative spikes respectively. The event images also show the effect of varying the contrast threshold  $\tau$  and exponential decay  $\beta$ —larger values yield a less noisy but sparser event stream.

provide extreme high-speed video imaging. Fig. 3 (right) shows the modulating masks for a four-bucket capture.

### 5.2. Event Cameras

Next, we describe the emulation of event cameras, which capture changes in light intensity and are conceptually similar to the temporal contrast projection introduced in Eq. (5). Physical implementations of event sensors [6, 14, 36, 60] generate a photoreceptor voltage  $V(\mathbf{x}, t)$  with a logarithmic response to incident flux  $\Phi(\mathbf{x}, t)$ , and output an event  $(\mathbf{x}, t, p)$  when this voltage deviates sufficiently from a reference voltage  $V_{\text{ref}}(\mathbf{x})$ :

$$|V(\mathbf{x}, t) - V_{\text{ref}}(\mathbf{x})| > \tau, \quad (7)$$

where  $\tau$  is called the contrast-threshold and  $p = \text{sign}(V(\mathbf{x}, t) - V_{\text{ref}}(\mathbf{x}))$  encodes the polarity of the event. Once an event is generated,  $V_{\text{ref}}(\mathbf{x})$  is updated to  $V(\mathbf{x}, t)$ . Eq. (7), for a smoothly-varying flux intensity, thresholds a function of the temporal gradient, i.e.,  $\partial_t \log(\Phi(\mathbf{x}, t))$ .

**From bit-planes to event streams.** To produce events from SPAD frames, we compute an exponential moving average (EMA) of the bit-planes, as  $\mu_t(\mathbf{x}) = (1 - \beta)B_t(\mathbf{x}) + \beta\mu_{t-1}(\mathbf{x})$ —where  $\mu_t(\mathbf{x})$  is the EMA,  $\beta$  is the smoothing

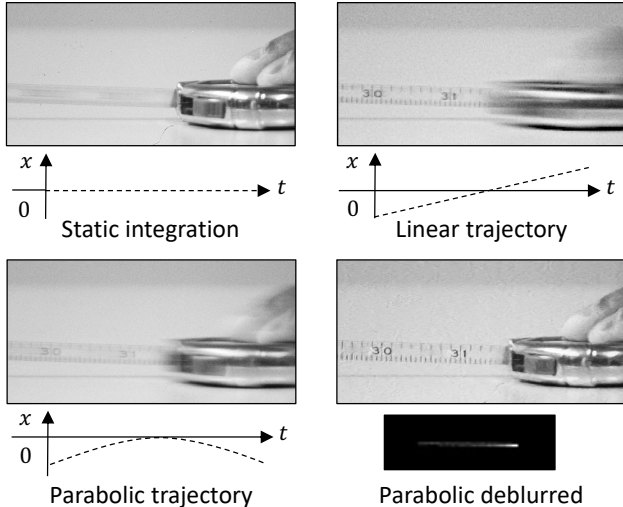


Figure 5: **Motion projections.** (*top*) Integrating along a linear trajectory in the photon-cube changes the apparent image-space velocity of scene objects. Details are seen for (*top left*) the case when static, and (*top right*) the metallic tape when the sensor translates along the  $x$ -axis. (*bottom*) A parabolic integration trajectory results in a motion-invariant image, resulting in similar blur kernels for all objects. (*bottom right*) Deblurring with the resultant shift-invariant point spread function (shown in *inset*) produces a sharp image.

factor, and  $B_t$  is a bit-plane. We generate an event when  $\mu_t(\mathbf{x})$  deviates from  $\mu_{\text{ref}}(\mathbf{x})$  by at least  $\tau$ :

$$|h(\mu_t(\mathbf{x})) - h(\mu_{\text{ref}}(\mathbf{x}))| > \tau, \quad (8)$$

where  $h$  is a scalar function applied to the EMA. We can see that Eq. (8) thresholds temporal contrast, by observing the role played by the EMA and the difference operator.

Setting  $h$  to be the logarithm of the flux MLE mimics Eq. (7). However, since the log-scale is used to prevent sensor saturation, a simpler alternative is to use the non-saturating response curve of SPAD pixels ( $h(x) = x$ ). The response curve takes the form of  $1 - \exp(-\alpha\Phi(\mathbf{x}, t))$ , where  $\alpha$  is a flux-independent constant. As a major advantage, this response curve avoids the underflow issues of the log function that can occur in low-light scenarios [62].

The SPAD’s frame rate determines the time-stamp resolution of emulated events. In Fig. 4, we show the events generated from a photon-cube acquired at a frame-rate of 96.8 kHz—resulting in a time-stamp resolution of  $\sim 10 \mu\text{s}$  that is comparable to those of existing event cameras.

**How do SPAD-events differ from the output of a regular event camera?** The main difference is the expression of temporal contrast, given by  $\partial_t h$ , is now  $-\partial_t \exp(-\alpha\Phi(\mathbf{x}, t))$ , instead of  $\partial_t \log(\Phi(\mathbf{x}, t))$ . This dif-

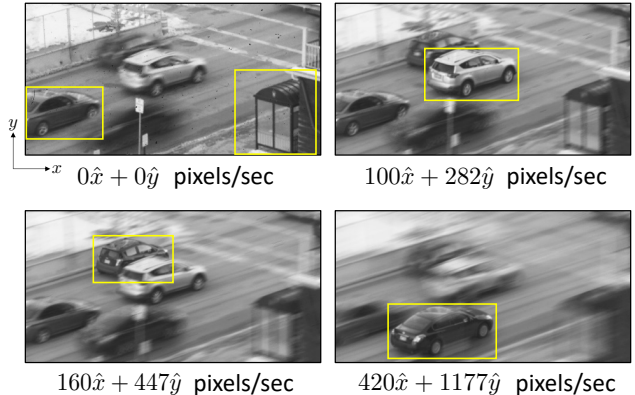


Figure 6: **Motion stack.** Computing multiple linear projections with different trajectories can produce a stack of images where objects with matching velocities are sharp. Here, we show a traffic scene involving four cars that have four different velocities. By suitably altering the slope of the linear trajectory, we can produce images where only one of the cars appears sharp at a time. We indicate the slope of the trajectories chosen and the objects that are “in-focus”.

ference poses no compatibility issues for a large class of event-vision algorithms that utilize a grid of events [13, 57, 66] or brightness changes [18]. We show examples of downstream applications using SPAD-events in Suppl. Sec. 2. Finally, SPAD-events can be easily augmented with spatially- and temporally-aligned intensity information—a synergistic combination that has been exploited by several recent event-vision works [18, 25, 74].

### 5.3. Motion Projections

Having described the emulation of cameras that capture coded exposures and temporal contrasts, we now shift our attention to cameras that emulate sensor motion during exposure, *viz.* motion cameras. We describe two useful trajectories when emulating motion cameras using Eq. (6).

**Linear trajectory.** The simplest sensor trajectory involves linear motion, where  $\mathbf{r}(t) = (bt + c) \hat{\mathbf{p}}$  for some constants  $b, c \in \mathbb{R}$  and unit vector  $\hat{\mathbf{p}}$ . As Fig. 5 (*top row*) shows, this can change the scene’s frame of reference: making moving objects appear stationary and vice-versa.

**Motion-invariant parabolic projection.** If motion is along  $\hat{\mathbf{p}}$ , parabolic integration produces a motion-invariant image [33]—all objects, irrespective of their velocity, are blurred by the same point spread function (PSF), up to a linear shift. Thus, a deblurred parabolic capture produces a sharp image of all velocity groups (Fig. 5 (*bottom row*)). The parabolic trajectory is given by  $\mathbf{r}(t) = (at^2 + bt + c) \hat{\mathbf{p}}$ . We choose  $a$  based on the maximum object velocity and  $b, c$

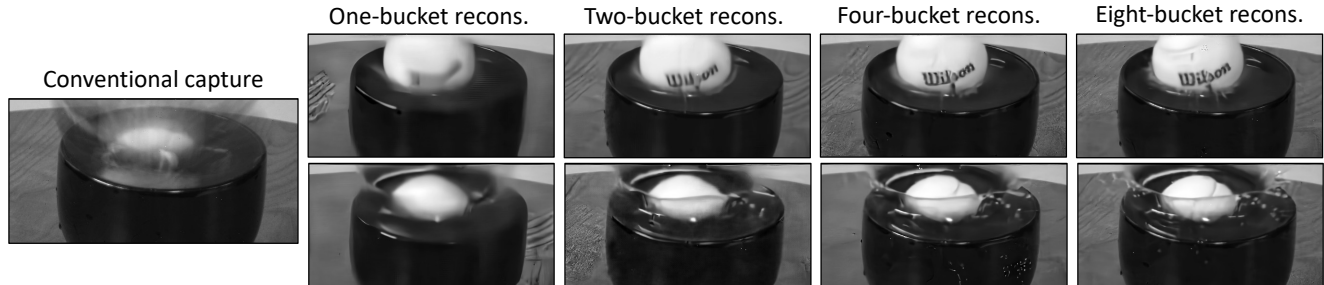


Figure 7: **High-speed videography at 2000 FPS** of a tennis ball dropped into a bowl of water, from a 25 Hz readout. The conventional capture provides a visualization of the scene dynamics. It is challenging to reconstruct a large number of frames from a single compressive snapshot. Multi-bucket captures recover frames with significantly greater detail, such as the crown of water surrounding the ball. **We include more sequences (e.g., a bursting balloon) in the supplementary material.**

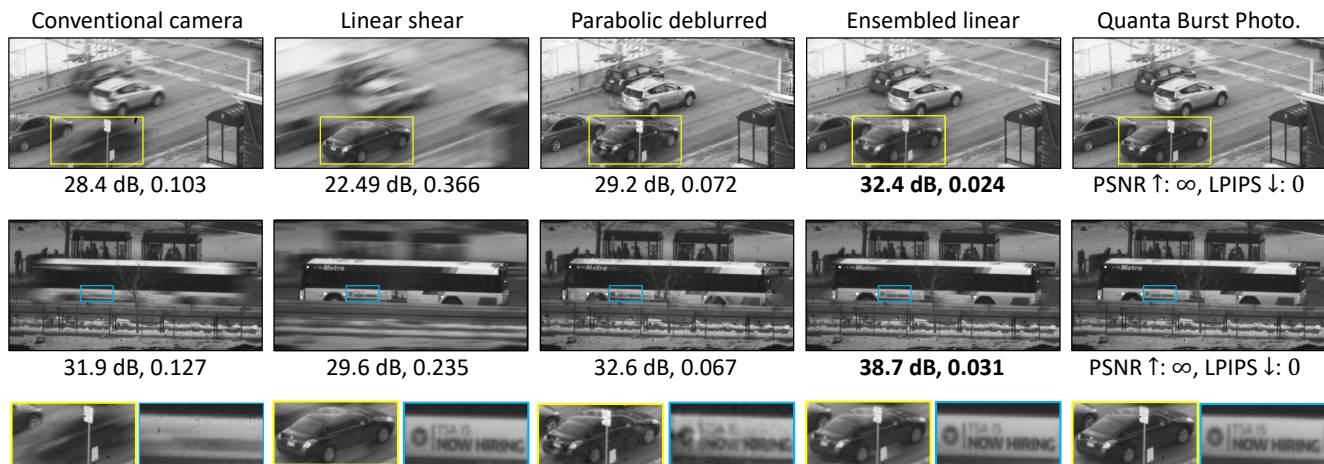


Figure 8: **Deblurring of traffic scenes using motion projections.** Linear projections can recover details of moving objects if their velocity is known. When only the motion direction is known (e.g., road’s orientation), a sharp image can be obtained by either deblurring a parabolic projection or by blending multiple randomly-sampled linear projections. We quantitatively compare against the compute- and bandwidth-expensive Quanta Burst Photography [11], based on PSNR and LPIPS [76].

so the parabola’s vertex lies at  $T/2$ . We readily obtain the PSF by applying the parabolic integration to a delta input. Upon deconvolution using the PSF, a parabolic projection provides the optimal SNR for a blur-free image from single capture when only the direction of velocity is known.

**Ensembling linear projections.** Finally, we leverage the flexibility of photon-cubes to compute multiple linear projections, as seen in Fig. 6. This produces a stack of images where one velocity group is motion-blur free at a time—or a ‘motion stack’, analogous to a focal stack. This novel construct can be used to compensate motion by blending stack images using cues such as blur orientation or optical flow.

## 6. Hardware and Experimental Results

We design a range of experiments to demonstrate the versatility of photon-cube projections: both when computa-

tions occur after readout (Secs. 6.1 and 6.2), and when they are performed near-sensor on-chip (Sec. 6.3). All photon-cubes were acquired using the SwissSPAD2 array [19], operated using one of two sub-arrays, each having  $512 \times 256$  pixels, and at a frame-rate of 96.8 kHz. For the on-chip experiments, we use the UltraPhase compute architecture to interface with photon-cubes acquired by the SwissSPAD2.

### 6.1. SoDaCam Capabilities

**High-speed compressive imaging.** We reconstruct 80 frames from compressive snapshots that are emulated at 25 Hz, resulting in a 2000 FPS video. We decode compressive snapshots using a plug-and-play (PnP) approach, PnP-FastDVDNet [26]. As Fig. 7 shows, it is challenging to recover a large number of frames from a single compressive measurement. Using the proposed multi-bucket scheme significantly improves the quality of video reconstruction.

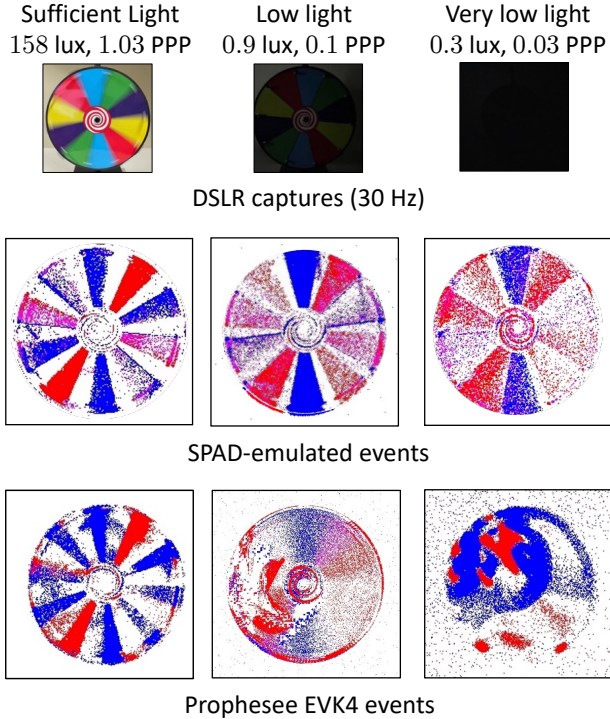


Figure 9: **Comparison to a state-of-the-art event camera.** SPAD-events can capture temporal gradients even when the light-level is reduced by  $500\times$ , by benefiting from their single-photon sensitivity and bounded brightness response curve. In contrast, low-light induces blur and deteriorates the Prophesee’s event stream. As a measure of the light-level, we report the PPP (photons per pixel) averaged across bit-planes and a light meter’s reading at the sensor location.

While multi-bucket captures require more bandwidth, this can be partially amortized by coding only dynamic regions, which we show in Suppl. Sec. 1.

**Motion projections on a traffic scene.** Fig. 8 shows two traffic scenes captured using a 50 mm focal length lens and at 30 Hz emulation. When object velocity is known, a linear projection can make moving objects appear stationary. If only the velocity direction is known (e.g., road’s orientation in Fig. 8), a parabolic projection provides a sharp reconstruction of all objects. We deblur parabolic captures using PnP-DnCNN [75]. We offer an improvement by randomly sampling 8 linear projections along the velocity direction and blending them using the optical flow predicted by RAFT [17] between two short exposures.

**Low-light event imaging.** Fig. 9 compares event-image visualizations of SPAD and that of a state-of-the-art commercial event sensor (Prophesee EVK4), across various

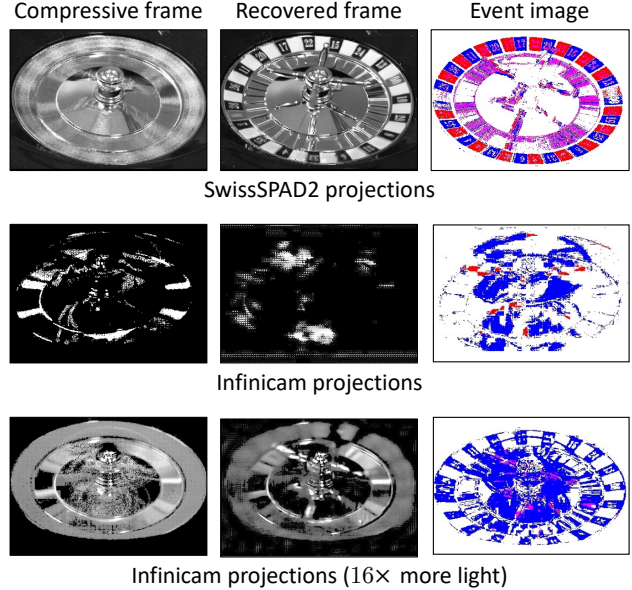


Figure 10: **Comparison against conventional high-speed acquisition at 4000 Hz.** (top) SPAD projections recover a  $16\times$  compressive video and an event image of a spinning roulette wheel. (middle) Read-noise corrupts the incident flux in the Infinicam high-speed camera, removing details in frames which are compressed on-the-fly. (bottom) Although using a larger aperture to admit more light recovers some detail, noise and compression artifacts still persist.

light levels, with an accumulation period of 33 ms. For a fair comparison, we bin the Prophesee’s events in blocks of  $2 \times 2$  pixels and use a smaller aperture to account for the lower fill factor of the SPAD. We tuned event-generation parameters (contrast threshold, integrator decay rate) of both cameras at each light level. Low light induces blur and deteriorates the Prophesee’s event stream. In contrast, SPAD-events continue to capture temporal gradients, due to the SPAD’s low-light capabilities and its brightness-encoding response curve. We include an ablation study of brightness-encoding functions in Suppl. Sec. 2.

Our observations are in concurrence with recent works that examine the low-light performance of event cameras [19, 27], and show that SPAD-events can provide neuromorphic vision in these challenging-SNR scenarios.

## 6.2. Comparison to High-Speed Cameras

Recall, as previously discussed in Sec. 4, that read-noise limits the per-frame SNR of high-speed cameras. To demonstrate this limitation, we compute projections using the 4 kHz acquisition of the Photron Infinicam, a conventional high-speed camera, at a resolution of  $1246 \times 240$  pixels. We operate the SwissSPAD2 and the Infinicam at ambient light conditions using the same lens specifications. As

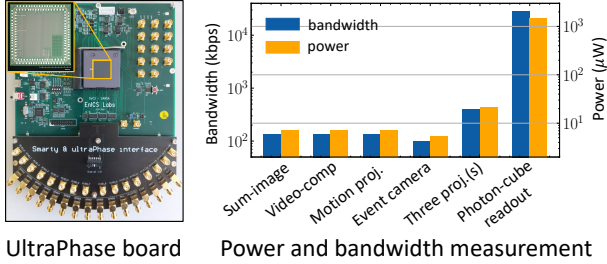


Figure 11: **Power and bandwidth requirements** when computing photon-cube projections on UltraPhase [1] (left), a recent compute architecture designed for single-photon imaging, at 40 Hz readout. (right) Our projections act as a compression scheme for photon-cubes, resulting in dramatically reduced sensor readout and power consumption.

Fig. 10 shows, read noise corrupts the incident signal in Infinicam and makes it impossible to derive any useful projections. The read noise could be averaged out to some extent if the Infinicam did not perform compression-on-the-fly, but compression is central to the camera’s working and enables readout over USB. Using a larger aperture to admit more light improves the quality of computed projections, but the video reconstruction and event image remain considerably worse than the corresponding outputs of the SPAD.

### 6.3. Bandwidth and Power Implications

While Sec. 6.1 has demonstrated the capabilities of photon-cube projections, we now show that our projections can also be obtained in a bandwidth-efficient manner via near-sensor computations. We implement photon-cube projections on UltraPhase (Fig. 11 (left)), a novel compute architecture designed for single-photon imaging. UltraPhase consists of  $3 \times 6$  processing cores, each of which interfaces with  $4 \times 4$  pixels, and can be 3D stacked beneath a SPAD array. We include visualizations and programming details of a few example projections in Suppl. Sec. 5.

We measure the readout and power consumption of UltraPhase when computing projections on 2500 bit-planes of the falling die sequence (Fig. 1). The projections include: VCS with 16 random binary masks, an event camera, a linear projection, and a combination of the three. We output projections at 12-bit depth and calculate metrics based on the clock cycles required for both compute and readout. As seen in Fig. 11 (right), computing projections on-chip dramatically reduces sensor readout and power consumption as compared to reading out the photon-cube. Finally, similar to existing event cameras, SPAD-events have a resource footprint that reflects the underlying scene dynamics.

In summary, our on-chip experiments show that performing computations near-sensor can increase the viability of single-photon imaging in resource-constrained settings.

## 7. Discussion and Future Outlook

SoDaCam provides a realization of reinterpretable software-defined cameras [2, 3, 20, 34, 51] at the fine temporal resolution of SPAD-acquired photon-cubes. The proposed computations, or photon-cube projections, can match and in some cases, surpass the capabilities of existing imaging systems. The software-defined nature of photon-cube projections provides functionalities that may be difficult to achieve in conventional sensors. These projections can reduce the readout and power-consumption of SPAD arrays and potentially spur widespread adoption of single-photon imaging in the consumer domain. Finally, future chip-to-chip communication standards may also make it feasible to compute projections on a camera image signal processor.

**Adding color to SoDaCam.** One way to add color is by overlaying color filter arrays (CFAs) and perform demosaicing on the computed photon-cube projection: depending on the projection, demosaicing could be relatively simple or more complex. As a reference, Bayer CFAs have been considered in the context of both video compressive sensing [26] and event cameras [64]. Incorporating CFAs with motion projections requires careful considerations, e.g., avoiding integrating across pixel locations of differing color.

**Future outlook on SPAD characteristics.** A key SPAD characteristic that determines several properties of emulated cameras is the frame rate. While no fundamental limitations prevent SPADs from being operated at the frame rates utilized in this work ( $\sim 100$  kHz), sensor readout and power constraints can preclude high speeds, especially in high-resolution SPAD arrays. Photon-cube projections can enable future large-format SPADs to preserve high-speed information with modest resource requirements.

**A platform for comparing cameras.** Comparing imaging modalities can be quite challenging since hardware realizations of sensors can differ in numerous aspects, such as their quantum efficiency, fill factor, pixel pitch, and array resolution. By emulating their imaging models, SoDaCam can serve as a platform for hardware-agnostic comparisons; for instance, determining operating conditions where one imaging modality is advantageous over another.

**A Cambrian explosion of new cameras.** Besides comparing cameras, by virtue of being software-defined, SoDaCam can also make it significantly easier to prototype and deploy new unconventional imaging models, and even facilitate sensor-in-the-loop optimization [44, 47, 63] by tailoring photon-cube projections for downstream computer-vision tasks. This is an exciting future line of research.

## References

- [1] Phantom-v2640. <https://www.phantomhighspeed.com/products/cameras/ultrahigh4mpx/v2640>. Accessed: 2023-01-28.
- [2] E. H. Adelson, J. R. Bergen, et al. The plenoptic function and the elements of early vision. *Computational models of visual processing*, 1(2):3–20, 1991.
- [3] A. Agrawal, A. Veeraraghavan, and R. Raskar. Reinterpretable imager: Towards variable post-capture space, angle and time resolution in photography. In *Computer Graphics Forum*, volume 29, pages 763–772. Wiley Online Library, 2010.
- [4] I. M. Antolovic, S. Burri, C. Bruschini, R. Hoebe, and E. Charbon. Nonuniformity analysis of a 65-kpixel CMOS SPAD imager. *IEEE Transactions on Electron Devices*, 63(1):57–64, 2016. doi: 10.1109/TED.2015.2458295.
- [1] A. Ardelean. *Computational Imaging SPAD Cameras*. PhD thesis, École polytechnique fédérale de Lausanne, 2023.
- [6] A. Boukhayma, A. Peizerat, and C.ENZ. A sub-0.5 electron read noise VGA image sensor in a standard CMOS process. *IEEE Journal of Solid-State Circuits*, 2016.
- [7] J. Canny. A computational approach to edge detection. *IEEE Transactions on Pattern Analysis and Machine Intelligence*, PAMI-8(6):679–698, 1986. doi: 10.1109/TPAMI.1986.4767851.
- [8] S. J. Carey, A. Lopich, D. R. Barr, B. Wang, and P. Dudek. A 100,000 fps vision sensor with embedded 535GOPS/W 256×256 SIMD processor array. In *2013 Symposium on VLSI Circuits*, pages C182–C183, 2013.
- [9] J. Chen, S. J. Carey, and P. Dudek. Feature extraction using a portable vision system. In *IEEE/RSJ Int. Conf. Intell. Robots Syst., Workshop Vis.-based Agile Auton. Navigation UAVs*, volume 2, 2017.
- [6] S. Chen and M. Guo. Live demonstration: Celex-v: A 1m pixel multi-mode event-based sensor. In *Proceedings of the IEEE/CVF Conference on Computer Vision and Pattern Recognition (CVPR) Workshops*, June 2019.
- [11] N. Dalal and B. Triggs. Histograms of oriented gradients for human detection. In *2005 IEEE computer society conference on computer vision and pattern recognition (CVPR'05)*, volume 1, pages 886–893. Ieee, 2005.
- [12] P. E. Debevec and J. Malik. Recovering high dynamic range radiance maps from photographs. In *Proceedings of the 24th Annual Conference on Computer Graphics and Interactive Techniques*, page 369–378. ACM Press/Addison-Wesley Publishing Co., 1997. doi: 10.1145/258734.258884. URL <https://doi.org/10.1145/258734.258884>.
- [13] F. M. Della Rocca, H. Mai, S. W. Hutchings, T. Al Abbas, K. Buckbee, A. Tsiamis, P. Lomax, I. Gyongy, N. A. Dutton, and R. K. Henderson. A 128×128 SPAD motion-triggered time-of-flight image sensor with in-pixel histogram and column-parallel vision processor. *IEEE Journal of Solid-State Circuits*, 55(7):1762–1775, 2020.
- [14] T. Finatou, A. Niwa, D. Matolin, K. Tsuchimoto, A. Mascheroni, E. Reynaud, P. Mostafalu, F. Brady, L. Chotard, F. LeGoff, H. Takahashi, H. Wakabayashi, Y. Oike, and C. Posch. 5.10 a 1280×720 back-illuminated stacked temporal contrast event-based vision sensor with 4.86µm pixels, 1.066GEPS readout, programmable event-rate controller and compressive data-formatting pipeline. In *2020 IEEE International Solid-State Circuits Conference - (ISSCC)*, pages 112–114, 2020. doi: 10.1109/ISSCC19947.2020.9063149.
- [15] E. R. Fossum. What to do with sub-diffraction-limit (SDL) pixels?—a proposal for a gigapixel digital film sensor (DFS). In *IEEE Workshop on Charge-Coupled Devices and Advanced Image Sensors*, pages 214–217, 2005.
- [16] E. R. Fossum. The quanta image sensor (QIS): Concepts and challenges. In *Imaging and Applied Optics*, page JTUe1. Optica Publishing Group, 2011. doi: 10.1364/COSI.2011.JTUe1. URL <http://opg.optica.org/abstract.cfm?URI=COSI-2011-JTUe1>.
- [17] E. R. Fossum, J. Ma, S. Masoodian, L. Anzagira, and R. Zizza. The quanta image sensor: Every photon counts. *Sensors*, 16(8):1260, 2016.
- [18] D. Gehrig, H. Rebecq, G. Gallego, and D. Scaramuzza. Eklt: Asynchronous photometric feature tracking using events and frames. *International Journal of Computer Vision*, 128(3):601–618, 2020.
- [19] R. Graca and T. Delbruck. Unraveling the paradox of intensity-dependent DVS pixel noise. *arXiv preprint arXiv:2109.08640*, 2021.
- [20] M. Gupta, A. Agrawal, A. Veeraraghavan, and S. G. Narasimhan. Flexible voxels for motion-aware videography. In *Computer Vision—ECCV 2010: 11th European Conference on Computer Vision, Heraklion, Crete, Greece, September 5–11, 2010, Proceedings, Part I 11*, pages 100–114. Springer, 2010.
- [21] F. Gutierrez-Barragan, A. Ingle, T. Seets, M. Gupta, and A. Velten. Compressive single-photon 3D cameras. In *Proceedings of the IEEE/CVF Conference on Computer Vision and Pattern Recognition (CVPR)*, pages 17854–17864, June 2022.
- [22] I. Gyongy, N. A. Dutton, and R. K. Henderson. Single-photon tracking for high-speed vision. *Sensors*, 18(2):323, 2018.
- [23] I. Gyongy, S. W. Hutchings, A. Halimi, M. Tyler, S. Chan, F. Zhu, S. McLaughlin, R. K. Henderson, and J. Leach.

- High-speed 3D sensing via hybrid-mode imaging and guided upsampling. *Optica*, 7(10):1253–1260, 2020.
- [24] C. Harris, M. Stephens, et al. A combined corner and edge detector. In *Alvey vision conference*, volume 15, pages 10–5244. Citeseer, 1988.
- [25] J. Hidalgo-Carrió, G. Gallego, and D. Scaramuzza. Event-aided direct sparse odometry. In *Proceedings of the IEEE/CVF Conference on Computer Vision and Pattern Recognition (CVPR)*, pages 5781–5790, June 2022.
- [26] B. K. Horn and B. G. Schunck. Determining optical flow. *Artificial intelligence*, 17(1-3):185–203, 1981.
- [27] Y. Hu, S.-C. Liu, and T. Delbruck. v2e: From video frames to realistic DVS events. In *Proceedings of the IEEE/CVF Conference on Computer Vision and Pattern Recognition (CVPR) Workshops*, pages 1312–1321, June 2021.
- [28] J. Igual. Photographic noise performance measures based on raw files analysis of consumer cameras. *Electronics*, 8(11):1284, 2019.
- [29] A. Ingle, A. Velten, and M. Gupta. High Flux Passive Imaging With Single-Photon Sensors. In *Proceedings of the IEEE/CVF Conference on Computer Vision and Pattern Recognition (CVPR)*, June 2019.
- [30] A. Ingle, T. Seets, M. Buttafava, S. Gupta, A. Tosi, M. Gupta, and A. Velten. Passive inter-photon imaging. In *Proceedings of the IEEE/CVF Conference on Computer Vision and Pattern Recognition (CVPR)*, June 2021.
- [31] K. Iwabuchi, Y. Kameda, and T. Hamamoto. Image quality improvements based on motion-based deblurring for single-photon imaging. *IEEE Access*, 9:30080–30094, 2021. doi: 10.1109/ACCESS.2021.3059293.
- [32] Y. Jiang, I. Choi, J. Jiang, and J. Gu. HDR video reconstruction with tri-exposure quad-bayer sensors. *arXiv preprint arXiv:2103.10982*, 2021.
- [33] A. Levin, P. Sand, T. S. Cho, F. Durand, and W. T. Freeman. Motion-invariant photography. *ACM Transactions on Graphics (TOG)*, 27(3):1–9, 2008.
- [34] M. Levoy and P. Hanrahan. Light field rendering. In *Proceedings of the 23rd annual conference on Computer graphics and interactive techniques*, pages 31–42, 1996.
- [9] Y. Li, M. Qi, R. Gulve, M. Wei, R. Genov, K. N. Kutulakos, and W. Heidrich. End-to-end video compressive sensing using anderson-accelerated unrolled networks. In *2020 IEEE International Conference on Computational Photography (ICCP)*, pages 1–12, 2020. doi: 10.1109/ICCP48838.2020.9105237.
- [36] P. Lichtsteiner. 64x64 event-driven logarithmic temporal derivative silicon retina. In *Program 2003 IEEE Workshop on CCD and AIS*, 2003.
- [37] Y. Liu, F. Gutierrez-Barragan, A. Ingle, M. Gupta, and A. Velten. Single-photon camera guided extreme dynamic range imaging. In *Proceedings of the IEEE/CVF Winter Conference on Applications of Computer Vision (WACV)*, pages 1575–1585, January 2022.
- [38] P. Llull, X. Liao, X. Yuan, J. Yang, D. Kittle, L. Carin, G. Sapiro, and D. J. Brady. Coded aperture compressive temporal imaging. *Opt. Express*, 21(9):10526–10545, May 2013. doi: 10.1364/OE.21.010526. URL <https://opg.optica.org/oe/abstract.cfm?URI=oe-21-9-10526>.
- [39] B. D. Lucas and T. Kanade. An iterative image registration technique with an application to stereo vision. In *IJCAI’81: 7th international joint conference on Artificial intelligence*, volume 2, pages 674–679, 1981.
- [40] J. Ma, S. Masoodian, D. A. Starkey, and E. R. Fossum. Photon-number-resolving megapixel image sensor at room temperature without avalanche gain. *Optica*, 4(12):1474–1481, Dec 2017. doi: 10.1364/OPTICA.4.001474. URL <http://www.osapublishing.org/optica/abstract.cfm?URI=optica-4-12-1474>.
- [11] S. Ma, S. Gupta, A. C. Ulku, C. Bruschini, E. Charbon, and M. Gupta. Quanta burst photography. *ACM Transactions on Graphics*, 39(4):1–16, July 2020. ISSN 0730-0301, 1557-7368.
- [42] S. Ma, P. Mos, E. Charbon, and M. Gupta. Burst vision using single-photon cameras. In *Proceedings of the IEEE/CVF Winter Conference on Applications of Computer Vision (WACV)*, pages 5375–5385, January 2023.
- [43] S. Mann and R. Picard. Beingundigital’ with digital cameras. *MIT Media Lab Perceptual*, 1:2, 1994.
- [44] J. N. Martel, L. K. Mueller, S. J. Carey, P. Dudek, and G. Wetzstein. Neural sensors: Learning pixel exposures for HDR imaging and video compressive sensing with programmable sensors. *IEEE Transactions on Pattern Analysis and Machine Intelligence*, 42(7):1642–1653, 2020.
- [45] J. N. P. Martel, L. K. Müller, S. J. Carey, and P. Dudek. Parallel HDR tone mapping and auto-focus on a cellular processor array vision chip. In *2016 IEEE International Symposium on Circuits and Systems (ISCAS)*, pages 1430–1433, 2016. doi: 10.1109/ISCAS.2016.7527519.
- [46] J. N. P. Martel, L. K. Müller, S. J. Carey, and P. Dudek. High-speed depth from focus on a programmable vision chip using a focus tunable lens. In *2017 IEEE International Symposium on Circuits and Systems (ISCAS)*, pages 1–4, 2017. doi: 10.1109/ISCAS.2017.8050548.
- [47] C. A. Metzler, H. Ikoma, Y. Peng, and G. Wetzstein. Deep optics for single-shot high-dynamic-range imaging. In *Proceedings of the IEEE/CVF Conference on Computer Vision and Pattern Recognition (CVPR)*, June 2020.

- [48] K. Morimoto, A. Ardelean, M.-L. Wu, A. C. Ulku, I. M. Antolovic, C. Bruschini, and E. Charbon. Megapixel time-gated SPAD image sensor for 2D and 3D imaging applications. *Optica*, 7(4):346–354, Apr. 2020.
- [49] K. Morimoto, J. Iwata, M. Shinohara, H. Sekine, A. Abdelghafar, H. Tsuchiya, Y. Kuroda, K. Tojima, W. Endo, Y. Maehashi, Y. Ota, T. Sasago, S. Maekawa, S. Hikosaka, T. Kanou, A. Kato, T. Tezuka, S. Yoshizaki, T. Ogawa, K. Uehira, A. Ehara, F. Inui, Y. Matsuno, K. Sakurai, and T. Ichikawa. 3.2 megapixel 3D-stacked charge focusing SPAD for low-light imaging and depth sensing. In *2021 IEEE International Electron Devices Meeting (IEDM)*, pages 20.2.1–20.2.4, 2021. doi: 10.1109/IEDM19574.2021.9720605.
- [50] S. Namiki, S. Sato, Y. Kameda, and T. Hamamoto. Imaging method using multi-threshold pattern for photon detection of quanta image sensor. In *International Workshop on Advanced Imaging Technology (IWAIT) 2022*, volume 12177, page 1217702. SPIE, 2022.
- [51] S. K. Nayar, V. Branzoi, and T. E. Boult. Programmable imaging: Towards a flexible camera. *International Journal of Computer Vision*, 70:7–22, 2006.
- [52] C. Posch, D. Matolin, and R. Wohlgenannt. A QVGA 143 dB Dynamic Range Frame-Free PWM Image Sensor With Lossless Pixel-Level Video Compression and Time-Domain CDS. *IEEE Journal of Solid-State Circuits*, 46(1):259–275, 2011. doi: 10.1109/JSSC.2010.2085952.
- [53] R. Raskar, A. Agrawal, and J. Tumblin. Coded exposure photography: motion deblurring using fluttered shutter. In *Acm Siggraph 2006 Papers*, pages 795–804. 2006.
- [13] H. Rebecq, R. Ranftl, V. Koltun, and D. Scaramuzza. Events-to-video: Bringing modern computer vision to event cameras. In *Proceedings of the IEEE/CVF Conference on Computer Vision and Pattern Recognition (CVPR)*, June 2019.
- [55] D. Reddy, A. Veeraraghavan, and R. Chellappa. P2C2: Programmable pixel compressive camera for high speed imaging. In *CVPR 2011*, pages 329–336, 2011. doi: 10.1109/CVPR.2011.5995542.
- [56] X. Ren, P. W. Connolly, A. Halimi, Y. Altmann, S. McLaughlin, I. Gyongy, R. K. Henderson, and G. S. Buller. High-resolution depth profiling using a range-gated CMOS SPAD quanta image sensor. *Optics express*, 26(5):5541–5557, 2018.
- [57] C. Scheerlinck, H. Rebecq, D. Gehrig, N. Barnes, R. Mahony, and D. Scaramuzza. Fast image reconstruction with an event camera. In *Proceedings of the IEEE/CVF Winter Conference on Applications of Computer Vision (WACV)*, March 2020.
- [58] T. Seets, A. Ingle, M. Laurenzis, and A. Velten. Motion adaptive deblurring with single-photon cameras. In *Proceedings of the IEEE/CVF Winter Conference on Applications of Computer Vision (WACV)*, pages 1945–1954, January 2021.
- [59] M.-W. Seo, Y. Shirakawa, Y. Masuda, Y. Kawata, K. Kawagawa, K. Yasutomi, and S. Kawahito. 4.3 a programmable sub-nanosecond time-gated 4-tap lock-in pixel cmos image sensor for real-time fluorescence lifetime imaging microscopy. In *2017 IEEE International Solid-State Circuits Conference (ISSCC)*, pages 70–71, 2017. doi: 10.1109/ISSCC.2017.7870265.
- [60] T. Serrano-Gotarredona and B. Linares-Barranco. A  $128 \times 128$  1.5% contrast sensitivity 0.9% FPN  $3 \mu\text{s}$  latency 4 mW asynchronous frame-free dynamic vision sensor using transimpedance preamplifiers. *IEEE Journal of Solid-State Circuits*, 48(3):827–838, 2013.
- [14] P. Shedligeri, A. S, and K. Mitra. A unified framework for compressive video recovery from coded exposure techniques. In *Proceedings of the IEEE/CVF Winter Conference on Applications of Computer Vision (WACV)*, pages 1600–1609, January 2021.
- [62] C. Shi, N. Song, W. Li, Y. Li, B. Wei, H. Liu, and J. Jin. A review of event-based indoor positioning and navigation. 2022.
- [63] V. Sitzmann, S. Diamond, Y. Peng, X. Dun, S. Boyd, W. Heidrich, F. Heide, and G. Wetzstein. End-to-end optimization of optics and image processing for achromatic extended depth of field and super-resolution imaging. *ACM Transactions on Graphics (TOG)*, 37(4):114, 2018.
- [64] G. Taverni, D. Paul Moeys, C. Li, C. Cavaco, V. Motsnyi, D. San Segundo Bello, and T. Delbruck. Front and back illuminated dynamic and active pixel vision sensors comparison. *IEEE Transactions on Circuits and Systems II: Express Briefs*, 65(5):677–681, 2018. doi: 10.1109/TCSII.2018.2824899.
- [17] Z. Teed and J. Deng. Raft: Recurrent all-pairs field transforms for optical flow. In *European Conference on Computer Vision*, 2020.
- [66] S. Tulyakov, D. Gehrig, S. Georgoulis, J. Erbach, M. Gehrig, Y. Li, and D. Scaramuzza. Time lens: Event-based video frame interpolation. In *Proceedings of the IEEE/CVF Conference on Computer Vision and Pattern Recognition (CVPR)*, pages 16155–16164, June 2021.
- [19] A. C. Ulku, C. Bruschini, I. M. Antolovic, Y. Kuo, R. Ankri, S. Weiss, X. Michalet, and E. Charbon. A  $512 \times 512$  SPAD Image Sensor With Integrated Gating for Widefield FLIM. *IEEE Journal of Selected Topics in Quantum Electronics*, 25(1):1–12, Jan. 2019. ISSN 1077-260X, 1558-4542. doi: 10.1109/JSTQE.2018.2867439.
- [68] G. Wan, X. Li, G. Agranov, M. Levoy, and M. Horowitz. CMOS image sensors with multi-bucket pixels for computational photography. *IEEE Journal of Solid-State Circuits*, 47(4):1031–1042, 2012. doi: 10.1109/JSSC.2012.2185189.

- [69] M. Wei, N. Sarhangnejad, Z. Xia, N. Gusev, N. Katic, R. Genov, and K. N. Kutulakos. Coded two-bucket cameras for computer vision. In *Proceedings of the European Conference on Computer Vision (ECCV)*, September 2018.
- [70] M. White, S. Ghajari, T. Zhang, A. Dave, A. Veeraraghavan, and A. Molnar. A differential SPAD array architecture in 0.18  $\mu\text{m}$  CMOS for HDR imaging. In *2022 IEEE International Symposium on Circuits and Systems (ISCAS)*, pages 292–296, 2022. doi: 10.1109/ISCAS48785.2022.9937558.
- [71] T. Yamazaki, H. Katayama, S. Uehara, A. Nose, M. Kobayashi, S. Shida, M. Odahara, K. Takamiya, Y. Hisamatsu, S. Matsumoto, L. Miyashita, Y. Watanabe, T. Izawa, Y. Muramatsu, and M. Ishikawa. 4.9 a 1ms high-speed vision chip with 3D-stacked 140GOPS column-parallel PEs for spatio-temporal image processing. In *2017 IEEE International Solid-State Circuits Conference (ISSCC)*, pages 82–83, 2017. doi: 10.1109/ISSCC.2017.7870271.
- [72] F. Yang, Y. M. Lu, L. Sbaiz, and M. Vetterli. Bits from photons: Oversampled image acquisition using binary poisson statistics. *IEEE Transactions on Image Processing*, 21(4): 1421–1436, 2012. doi: 10.1109/TIP.2011.2179306.
- [26] X. Yuan, Y. Liu, J. Suo, F. Durand, and Q. Dai. Plug-and-play algorithms for video snapshot compressive imaging. *IEEE Transactions on Pattern Analysis and Machine Intelligence*, 44(10):7093–7111, 2022. doi: 10.1109/TPAMI.2021.3099035.
- [74] J. Zhang, X. Yang, Y. Fu, X. Wei, B. Yin, and B. Dong. Object tracking by jointly exploiting frame and event domain. In *Proceedings of the IEEE/CVF International Conference on Computer Vision (ICCV)*, pages 13043–13052, 2021.
- [75] K. Zhang, Y. Li, W. Zuo, L. Zhang, L. Van Gool, and R. Timofte. Plug-and-play image restoration with deep denoiser prior. *arXiv preprint*, 2020.
- [76] R. Zhang, P. Isola, A. A. Efros, E. Shechtman, and O. Wang. The unreasonable effectiveness of deep features as a perceptual metric. In *Proceedings of the IEEE Conference on Computer Vision and Pattern Recognition (CVPR)*, June 2018.
- [77] T. Zhang, M. J. White, A. Dave, S. Ghajari, A. Raghuram, A. C. Molnar, and A. Veeraraghavan. First arrival differential LiDAR. In *2022 IEEE International Conference on Computational Photography (ICCP)*, pages 1–12, 2022. doi: 10.1109/ICCP54855.2022.9887683.
- [78] W. Zhang and L. Lin. Light field flow estimation based on occlusion detection. *Journal of Computer and Communications*, 5(3):1–9, 2017.

# Supplementary Material for “SoDaCam: Software-defined Cameras via Single-Photon Imaging”

## 1. Video Compressive Sensing

In this supplementary note, we provide the pseudo code that describes the emulation of two- and multi-bucket cameras and mathematically describe their multiplexing masks. We also specify algorithmic details for video recovery from compressive measurements.

### Multi-Bucket Capture Pseudocode

Algorithm 1 describes the emulation of  $J$ -bucket captures, denoted as  $\mathcal{I}_{\text{coded}}^j(\mathbf{x})$ , from the photon-cube  $B_t(\mathbf{x})$  using multiplexing codes  $C_t^j(\mathbf{x})$ , where  $1 \leq j \leq J$ . Both single compressive snapshots (or one-bucket captures) and two-bucket captures can be emulated as special cases of Algorithm 1, with  $J = 1$  and  $J = 2$  respectively.

---

#### Algorithm 1 Multi-Bucket Capture Emulation

---

**Require:** Photon-cube  $B_t(\mathbf{x})$   
Number of buckets  $J$   
Multiplexing code for  $j^{\text{th}}$  bucket,  $1 \leq j \leq J$ ,  $C_t^j(\mathbf{x})$   
Pixel locations  $\mathcal{X}$   
Total bit-planes  $T$   
**Ensure:** Multiplexed captures  $\mathcal{I}_{\text{coded}}^j(\mathbf{x})$   
**function** MULTIBUCKETEMULATION( $B_t(\mathbf{x})$ ,  $C_t^j(\mathbf{x})$ )  
     $Y^j(\mathbf{x}) \leftarrow 0, \forall j$   
    **for**  $\mathbf{x} \in \mathcal{X}, 1 \leq j \leq J$  **do**  
        **for**  $1 \leq t \leq T$  **do**  
             $\mathcal{I}_{\text{coded}}^j(\mathbf{x}) \leftarrow \mathcal{I}_{\text{coded}}^j(\mathbf{x}) + B_t(\mathbf{x}) \cdot C_t^j(\mathbf{x})$   
        **end for**  
    **end for**  
    **return**  $\mathcal{I}_{\text{coded}}^j(\mathbf{x})$   
**end function**

---

**Mask sequences for video compressive sensing.** For a single compressive capture ( $J = 1$ ), a sequence of binary random is used, i.e,  $C_t^1(\mathbf{x}) = 1$  with probability 0.5. For a two bucket capture, we use

$$C_t^2(\mathbf{x}) = 1 - C_t^1(\mathbf{x}),$$

which is the complementary mask sequence. For  $J > 2$ , at each timestep  $t$  and pixel location  $\mathbf{x}$ , the active bucket is chosen at random:

$$C_t^j(\mathbf{x}) \leftarrow 1, j \sim \text{Uniform}(1, J).$$

This is a direct generalization of the masking used for both one- and two-bucket captures.

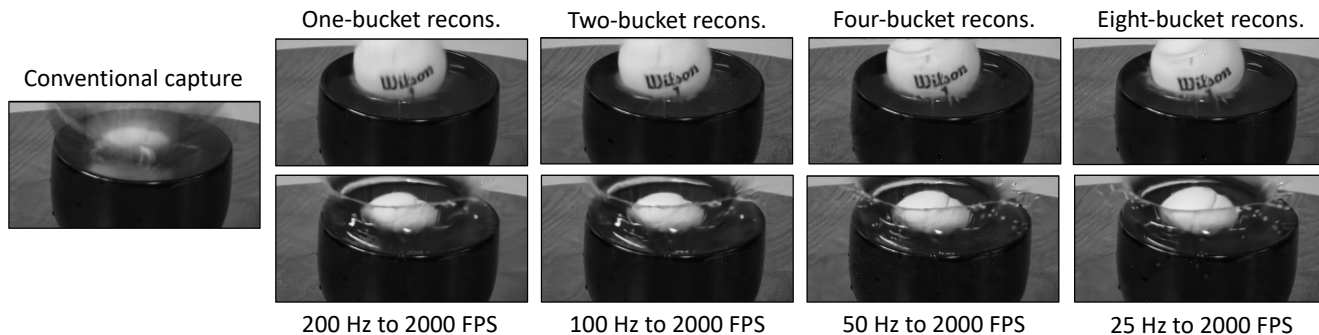
### Decoding Video Compressive Captures

A variety of decoding algorithms have been developed for video compressive sensing, including: (a) optimization frameworks tailored to the forward model of Eq. (4) and with additional regularization [10, 24], (b) end-to-end deep-learning methods that utilize a large corpus of training data [7, 9, 14, 22, 23], and (c) hybrid, plug-and-play (PnP) approaches that utilize an optimization framework but perform one or more steps using a deep denoiser [5, 20, 26]. We opt to use the PnP approach featuring an ADMM formulation [25] and a deep video denoiser (FastDVDNet [16]) in this work. We justify our choice by noting that PnP-ADMM can produce high-quality reconstructions, comparable to end-to-end counterparts while using an off-the-shelf denoiser—precluding the need to train separate models for various masking strategies.

For computational efficiency, PnP-ADMM requires the gram matrix of the resulting linear forward model of Eq. (4) to be efficiently invertible. The multi-bucket scheme described above adheres to this consideration.

## Constant-Bandwidth Comparison

We now present a comparison of single-, two- and multi-bucket compressive captures when the readout rate is fixed. As Supp. Fig. 1 shows, multi-bucket captures provide higher fidelity reconstructions even when bandwidth is fixed. Furthermore, their bandwidth cost can be amortized, to some extent, by coding only dynamic regions—we describe this next.



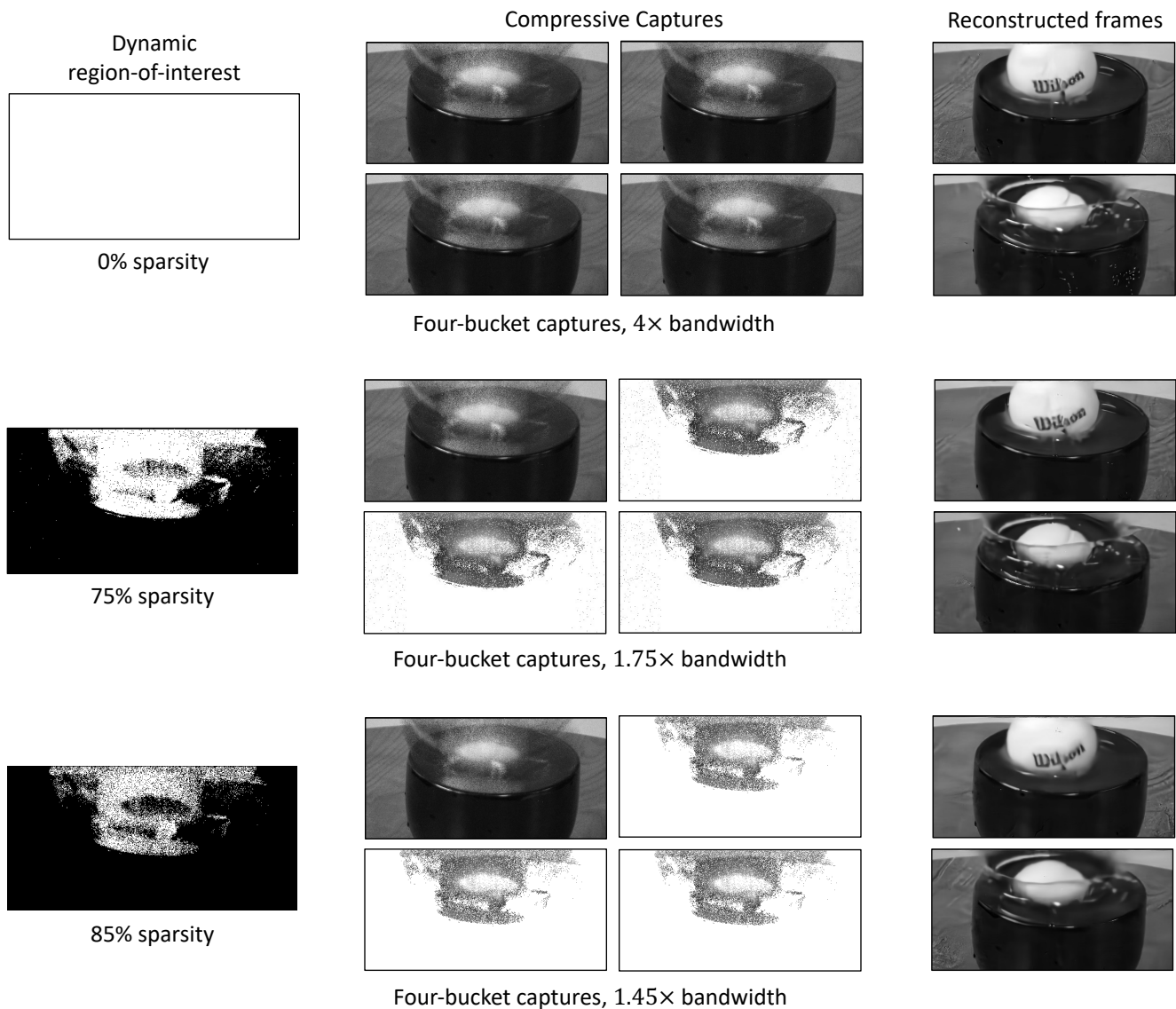
Supplementary Figure 1: **Fixed readout comparison of compressive video schemes.** We compare video reconstruction obtained from a single compressive snapshot, two-bucket capture, four-bucket capture and eight-bucket capture while holding readout constant—we achieve this by commensurately increasing readout, for instance, by reading out single compressive snapshots at 200 Hz. We indicate the readout rate here in Hertz (Hz) and the frame-rate of the reconstructed video in FPS. Clearly, multi-bucket captures provide better reconstruction results than a burst of independently multiplexed captures.

## Coding Only Dynamic Regions: Mitigating the Bandwidth Cost of Multi-Bucket Captures

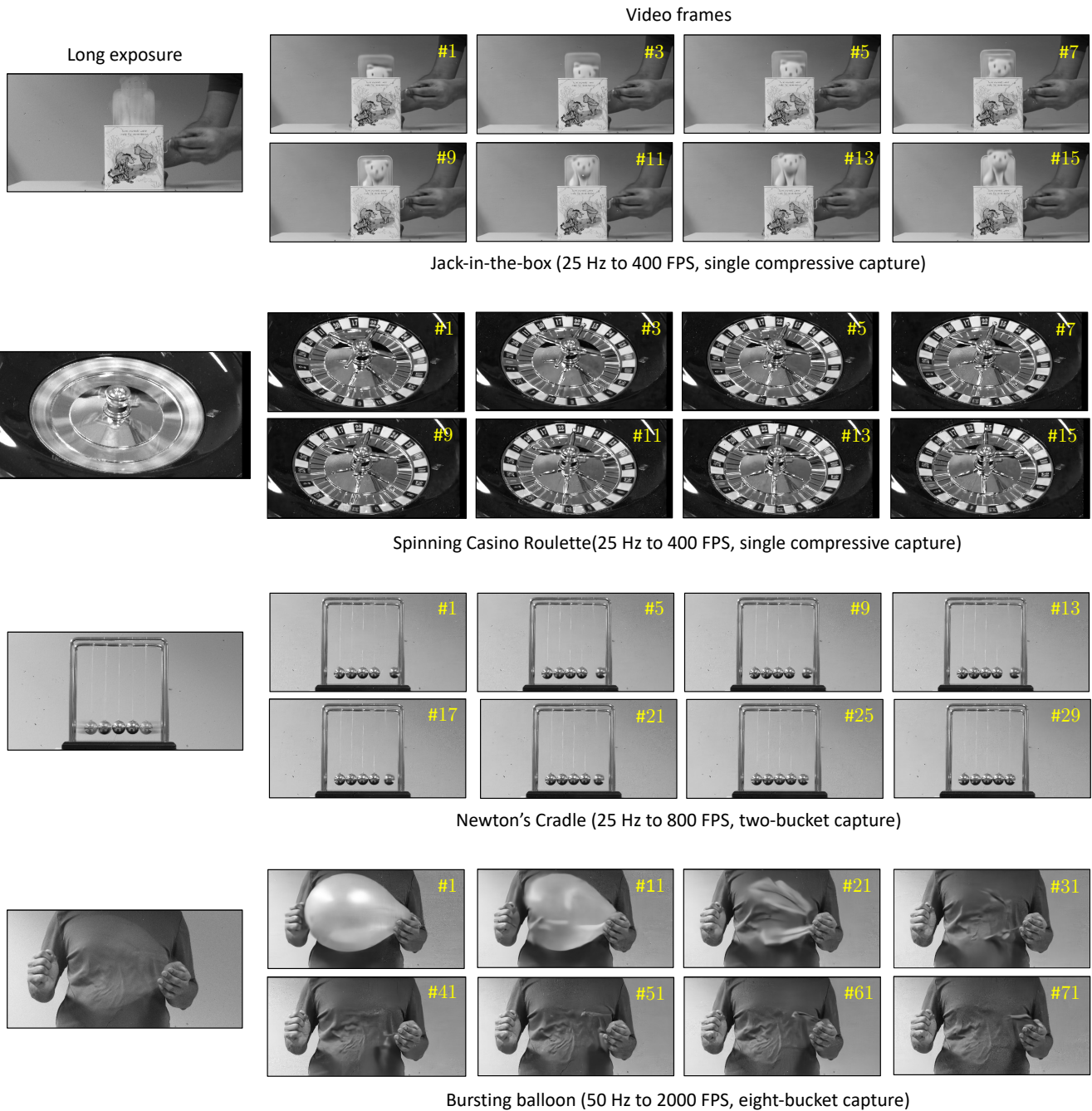
We observe that multi-bucket captures capture redundant information in static regions of the scene since each pixel in a static region has the same expected value under random binary modulation. Hence, we propose coding only dynamic regions—the dynamic region-of-interest (RoI) can be determined by masking pixels whose coded exposures deviate significantly from one another. As seen in Supp. Fig. 2, the dynamic content may just be 25% of the image area, which provides significant scope for bandwidth savings. We observe that we can code just 25% of the total pixels, among additional compressive measurements, without a perceptible drop in visual quality, which yields an overall bandwidth requirement of  $1.45\times$ , or under twice the bandwidth cost of a single compressive measurement.

## Results on More Sequences

Additional results are shown in Supp. Fig. 3.



Supplementary Figure 2: **Coding dynamic regions can reduce readout of multi-bucket captures.** (*left column*) Dynamic regions are detected by computing the standard deviation of the coded exposures and thresholding them appropriately (e.g., by the 75<sup>th</sup> percentile)—we show the dynamic regions in white here. Coded exposures are transmitted only in the dynamic regions. For the static regions, we simply use a long exposure—by adding multi-bucket captures. (*right column*) We observe that readout-bandwidth can be reduced to 1.75 $\times$  from 4 $\times$  in the case of a four-bucket capture with no perceptual degradation of reconstruction quality. Bandwidth is provided here as a multiple of the readout of a single compressive capture.



Supplementary Figure 3: **Results on additional sequences.** We use Hertz (Hz) to indicate the rate of emulation and frames-per-second (FPS) to indicate the frame-rate of the reconstructed video. Frame numbers are indicated in yellow font.

## 2. Event Cameras

### Event-Generation Pseudocode

We provide the pseudocode for emulating events from photon-cubes in Algorithm 2. The contrast threshold  $\tau$  and exponential smoothing factor  $\beta$  are the two parameters that determine the characteristics of the resulting event stream, such as its event rate (number of events per second). We use an initial time-interval  $T_0$  (typically 80–100 bit-planes) to initialize the reference moving average, with  $T_0$  being much smaller than  $T$ . The result of this pseudocode is an event-cube,  $E_t(\mathbf{x})$ , which is a sparse spatio-temporal grid of event polarities—positive spikes are denoted by 1 and negative spikes by  $-1$ . From the emulated event-cube, other event representations can be computed such as: an event stream,  $\{(\mathbf{x}, t, p)\}$ , where  $p \in \{-1, 1\}$  indicates the polarity of the event; a frame of accumulated events [12] (seen in Figs. 4 and 9); and a voxel grid representation [27], where events are binned into a few temporal bins (shown in Supp. Fig. 4 (top left) using 3 temporal bins).

---

**Algorithm 2** Event Camera Emulation

---

**Require:** Photon-cube  $B_t(\mathbf{x})$

Contrast threshold  $\tau$

Exponential smoothing factor,  $\beta$

Pixel locations  $\mathcal{X}$

Initial time-interval  $T_0$ , for computing reference moving average

Total bit-planes  $T$

**Ensure:** Event-cube  $E_t(\mathbf{x})$  that describes the spatio-temporal spikes

**function** EVENTCAMERAEMULATION( $B_t(\mathbf{x}), \tau, \beta, T_0$ )

$E_t(\mathbf{x}) \leftarrow 0, \forall t, \forall \mathbf{x}$

**for**  $\mathbf{x} \in \mathcal{X}$  **do**

Reference moving average,  $\mu_{\text{ref}}(\mathbf{x}) \leftarrow 0$

Current moving average,  $\mu_0(\mathbf{x}) \leftarrow 0$

**for**  $1 \leq t \leq T_0$  **do**

$\mu_{\text{ref}}(\mathbf{x}) \leftarrow \beta\mu_{\text{ref}}(\mathbf{x}) + (1 - \beta)B_t(\mathbf{x})$

**end for**

**for**  $T_0 \leq t \leq T$  **do**

$\mu_t(\mathbf{x}) \leftarrow \beta\mu_{t-1}(\mathbf{x}) + (1 - \beta)B_t(\mathbf{x})$

**if**  $|\mu_t(\mathbf{x}) - \mu_{\text{ref}}(\mathbf{x})| > \tau$  **then**

$E_t(\mathbf{x}) \leftarrow \text{sign}(\mu_t(\mathbf{x}) - \mu_{\text{ref}}(\mathbf{x}))$

$\mu_{\text{ref}}(\mathbf{x}) \leftarrow \mu_{\text{ref}}(\mathbf{x}) + \tau * \text{sign}(\mu_t(\mathbf{x}) - \mu_{\text{ref}}(\mathbf{x}))$

**end if**

**end for**

**end for**

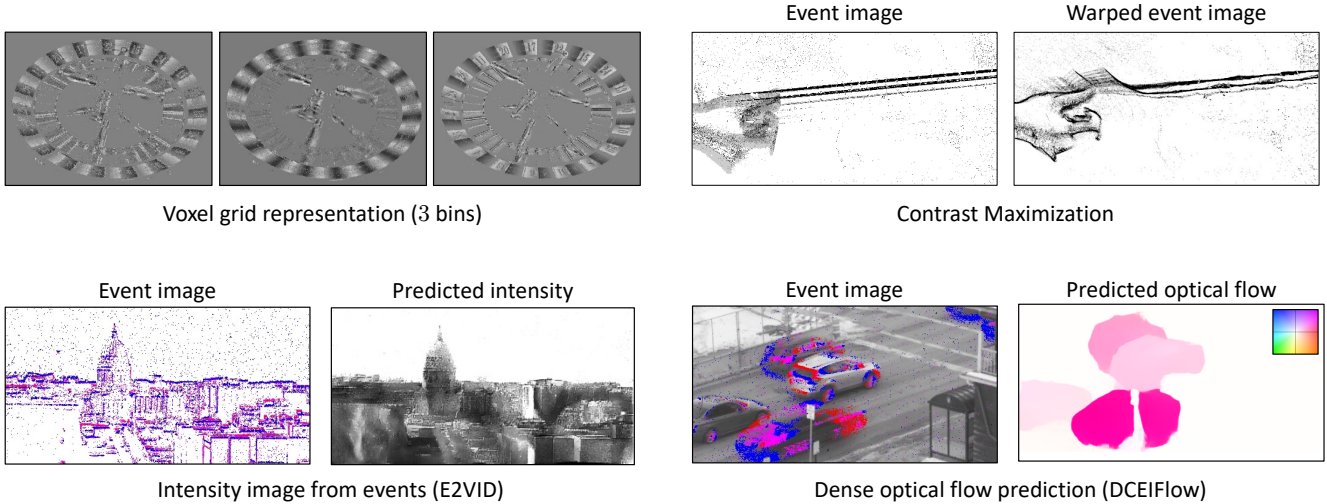
**return**  $E_t(\mathbf{x})$

**end function**

---

### Compatibility of SPAD-Events with Existing Event-Vision Algorithms

We now provide examples of downstream algorithms applied to SPAD-events, which shows the compatibility of the emulated event streams with existing event-vision algorithms. Supplementary Figure 4 shows three downstream algorithms with SPAD-events as their input: Contrast Maximization [8] which generates a warped image of events that has sharp edges (top right), E2VID [13] which estimates intensity frames from an event stream (bottom left), and DCEIFlow [21] which computes dense optical flow using intensity frames and aligned events (bottom right). Both E2VID and DCEIFlow use a voxel grid representation of events as their inputs. We include the visualization of a voxel grid representation in Supp. Fig. 4 (top left). All event streams were emulated using 3000 bit-planes of photon-cubes acquired at 96.8 kHz, and using  $\beta = 0.95$  and  $\tau = 0.4$  as emulation parameters. We note that the performance of these algorithms can be improved by finetuning pre-trained learning-based models on a dataset of SPAD-events.



Supplementary Figure 4: **Compatibility of SPAD-events with existing event-vision algorithms.** The flow field visualization follows Baker et al. [2]. The photon-cube for the contrast maximization output was obtained from Ma et al. [11].

### Ablation of Brightness-Encoding Functions

Our event emulation scheme (Algorithm 2) relies on the SPAD’s response curve to encode scene brightness, which is a non-linear and non-saturating response of the form

$$1 - \exp(-\alpha\Phi(\mathbf{x}, t)),$$

where  $\alpha = \eta t_{\text{exp}}$  and assuming negligible dark count rate (DCR). Current event cameras typically use a logarithmic response to encode scene brightness. This can also be utilized to emulate events from photon-cubes by setting  $h$  (as described in Eq. (8)) to be the log-MLE function:

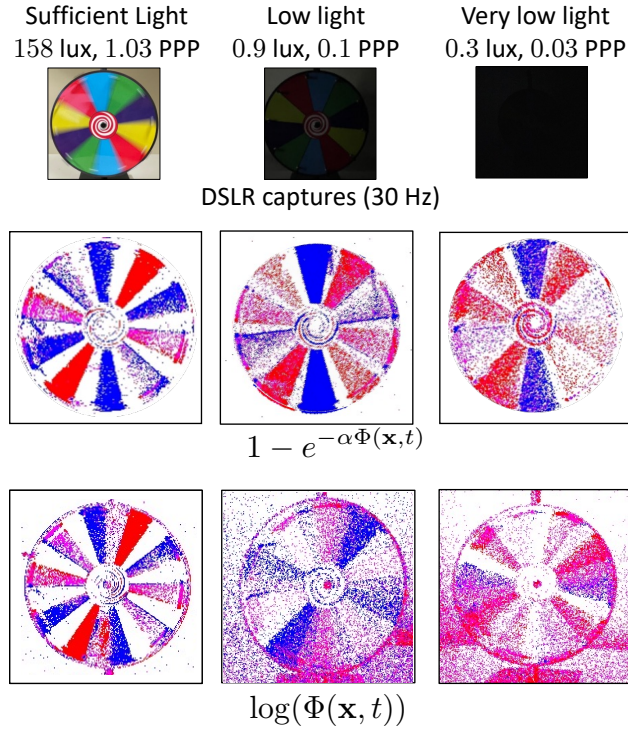
$$h(\mu) = \log\left(-\frac{\log(1 - \mu)}{\eta t_{\text{exp}}}\right).$$

However, a log-response suffers from underflow issues, particularly at low-light scenarios as seen in Supp. Fig. 5.

### SoDaCam Flexibility and SPAD-Events

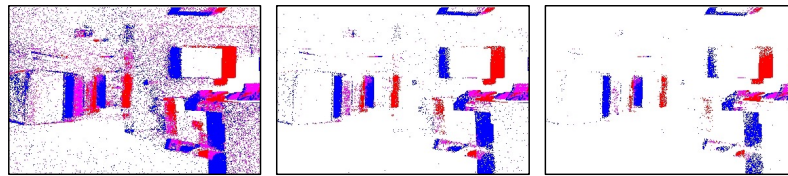
Here are a few benefits of the SoDaCam approach for event-based imaging:

- **Direct access to intensity information.** By computing a sum image, SoDaCam makes intensity frames that are spatially- and temporally-aligned with the generated event stream available. This precludes the need for multiple devices, which often require careful alignment and calibration.
- Further, the intensity frames obtained via the sum-image feature the SPAD’s imaging capabilities, i.e., such intensity frames feature a high dynamic range and can be utilized in low-light imaging scenarios. This is in contrast to dynamic active vision sensors (DAVIS) [3, 6], where a conventional frame, which has limited dynamic range and low-light capabilities compared to SPAD-derived images, can be obtained in addition to the event stream.
- **Computing multiple event-streams simultaneously.** Contrast threshold  $\tau$  is an important parameter that controls the sparsity and noise level of generated event stream: small values of  $\tau$  can produce potentially noisy event streams that require extensive processing, while large values of  $\tau$  can result in very sparse streams with less useful information. With SoDaCam, it is possible to emulate event streams with different values of  $\tau$  simultaneously, thereby amortizing these trade-offs. In fact, this can be thought of as analogous to exposure stacks but in the context of event-imaging. Supplementary Figure 6 (top row) shows an example of an ‘event-image stack’.

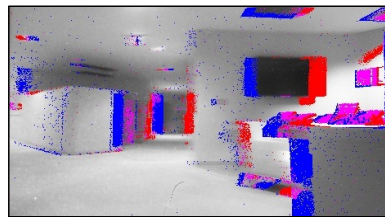


Supplementary Figure 5: **Comparison of brightness encoding functions.** While the log-MLE is comparable to using the SPAD’s response curve at ambient light levels, at low flux levels the underflow issues associated with the log function occur. Here,  $\alpha$  denotes a sensor-determined and flux-independent constant.

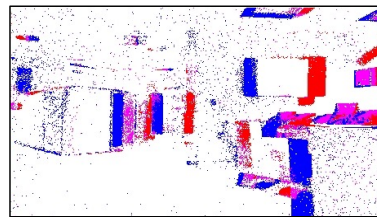
- **Per-pixel contrast thresholds.** We can also vary the contrast threshold  $\tau$  as a function of pixel location or incident intensity. For instance, we can use a smaller contrast threshold if we have an estimate of the incident intensity with less variance and a higher contrast threshold when there is more variance. We show an example of this in Supp. Fig. 4 (*bottom right*), where we vary the contrast threshold between 0.35 and 0.45 as a linear function of the sample variance of the moving average,  $\mu_t(\mathbf{x})$ .



Event stack (different contrast thresholds)



Events overlaid on image



Variance adaptive policy

Supplementary Figure 6: **Flexible event-based imaging.** (*top*) An ‘event-stack’ that employs increasing contrast thresholds,  $\tau = 0.35, 0.4, 0.45$ . (*bottom*) We can also output frames with aligned events, and use event generation policies that may not be trivial to realize in hardware—such as varying the contrast threshold  $\tau$  as a linear function of the sample variance.

### 3. Motion Projections

#### Pseudocode for Emulating Motion Cameras

Algorithm 3 provides the pseudocode for emulating sensor motion from a photon-cube, where the sensor’s trajectory is determined by the discretized function  $\mathbf{r}$ . At each time instant  $t$ , we shift bit-planes by  $\mathbf{r}(t)$  and accumulate them in  $\mathcal{I}_{\text{shift}}$ . For pixels that are out-of-bounds, no accumulation is performed. For this reason, the number of summations that occur varies spatially across pixel locations  $\mathbf{x}$ —we normalize the emulated shift-image by the number of pixel-wise accumulations  $N(\mathbf{x})$  to account for this. The function  $\mathbf{r}$  can be obtained by discretizing any smooth 2D trajectory: by either rounding up or dithering, or by using a discrete line-drawing algorithm [4].

---

#### Algorithm 3 Motion Camera Emulation

---

**Require:** Photon-cube  $B_t(\mathbf{x})$   
 Discretized trajectory  $\mathbf{r}(t)$   
 Pixel locations  $\mathcal{X}$   
 Total bit-planes  $T$

**Ensure:**  $\mathcal{I}_{\text{shift}}(\mathbf{x})$

**function** MOTIONCAMERAEMULATION( $B_t(\mathbf{x}), \mathbf{r}$ )  
    $\mathcal{I}_{\text{shift}}(\mathbf{x}) \leftarrow 0, \forall \mathbf{x}$   
   **for**  $\mathbf{x} \in \mathcal{X}$  **do**  
     Normalizer,  $N(\mathbf{x}) \leftarrow 0$   
     **for**  $1 \leq t \leq T$  **do**  
       **if**  $\mathbf{x} + \mathbf{r}(t) \in \mathcal{X}$  **then**  
          $N(\mathbf{x}) \leftarrow N(\mathbf{x}) + 1$   
          $\mathcal{I}_{\text{shift}}(\mathbf{x}) \leftarrow \mathcal{I}_{\text{shift}}(\mathbf{x}) + B_t(\mathbf{x} + \mathbf{r}(t))$   
       **end if**  
     **end for**  
     **if**  $N(\mathbf{x}) > 0$  **then**  
        $\mathcal{I}_{\text{shift}}(\mathbf{x}) \leftarrow \mathcal{I}_{\text{shift}}(\mathbf{x}) / N(\mathbf{x})$   
     **end if**  
   **end for**  
**return**  $\mathcal{I}_{\text{shift}}(\mathbf{x})$   
**end function**

---

As described in Sec. 5.3, we consider two trajectories: linear and parabolic. Linear trajectories are parameterized by their slope

$$\mathbf{r}(t) = v \left( t - \frac{T}{2} \right) \hat{\mathbf{p}},$$

where  $v$  is the object velocity,  $\hat{\mathbf{p}}$  is a unit vector that describes the trajectory’s direction, and  $T$  is the total number of bit-planes. Parabolic trajectories are parameterized by their maximum absolute slope,  $v_{\text{max}}$

$$\mathbf{r}(t) = \frac{v_{\text{max}}}{T} \left( t - \frac{T}{2} \right)^2 \hat{\mathbf{p}}.$$

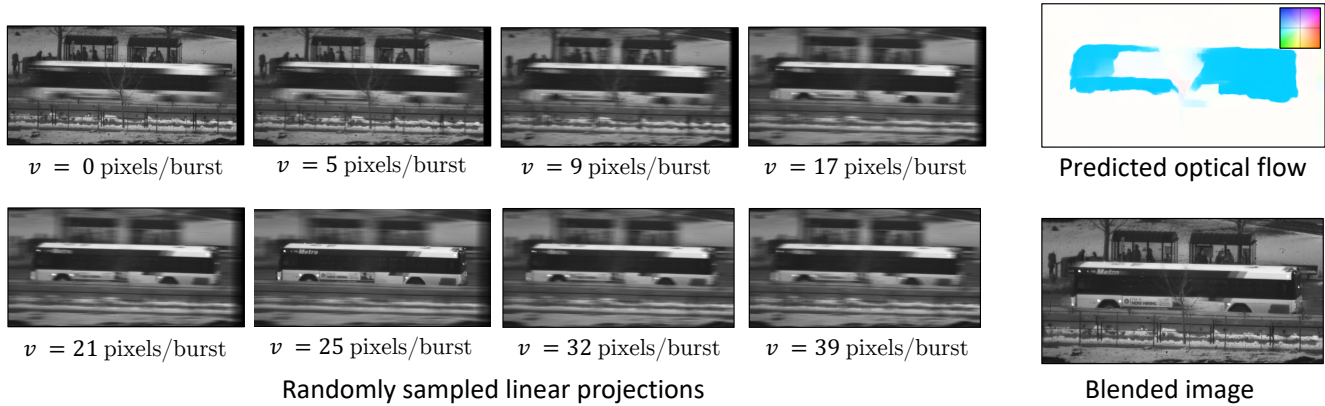
To prevent tail-clipping, which are image artifacts introduced by the finite extent of the parabolic integration, it is important to choose  $v_{\text{max}}$  to be sufficiently higher than the velocity of objects in the scene. Both linear and parabolic trajectories have a zero at  $t = T/2$ —which allows blending multiple linear projections without any pixel alignment issues.

#### Blending Multiple Linear Projections

As shown in Fig. 8, randomly sampling multiple linear projections (seen in Supp. Fig. 7 (left column)) can provide motion compensation when only the motion direction, and not the exact extent of motion, is known. To blend these projections, in addition to the randomly sampled linear projections, we also compute two short exposures using bit-planes at the beginning and end of the photon-cube. For the scenes shown in Fig. 8, we used the first 200 and the last 200 bit-planes to emulate short exposures. We then use RAFT [17] to predict optical flow between the two short exposures—which can be used to select the

linear projection that can best compensate motion as a function of the pixel location (as seen in Supp. Fig. 7 (*left column*)). We did not have to perform any spatial smoothing after selecting linear projections, since the optical flow predicted by RAFT was reasonably smooth.

Blending can also be achieved by choosing the least blurred linear projection in a per-pixel manner—similar to how focal stacking is typically achieved. This would however require predicting per-pixel blur kernels or constructing a measure of motion blur. Laplacian filters, which are typically used for focal stacking, do not readily work with motion stacks.



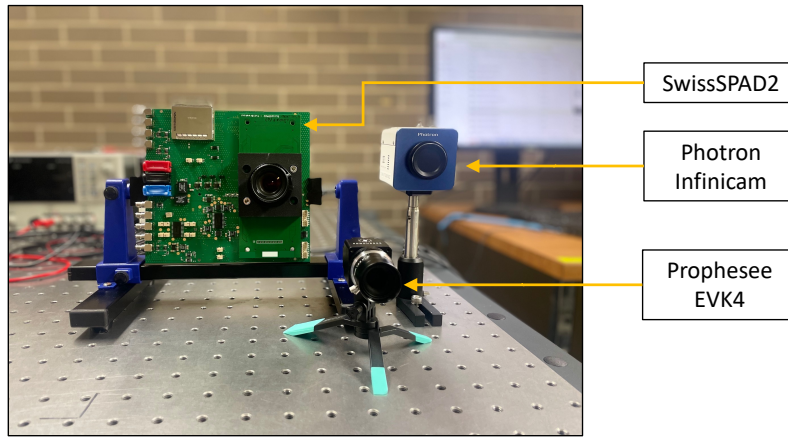
Supplementary Figure 7: **An example of motion stack blending.** (*left*) We sample 8 linear projections randomly along the road’s orientation such that their ensuing pixel displacements are uniformly between 0 and 40 pixels. (*right*) We then blend them using the optical flow field that is predicted between two short exposures computed from the same photon-cube. The flow field visualization follows Baker et al. [2].

## 4. Experimental Setup for Secs. 6.1 and 6.2

### Cameras and Sensory Arrays Used

We used the following imagers for our experiments described in Secs. 6.1 and 6.2:

- **SwissSPAD2 array** a  $512 \times 512$  SPAD array that can be operated at a maximum frame rate of 97 kHz. We operate the SwissSPAD2 in its ‘half-array’ mode: utilizing one of two sub-arrays, with a resolution of  $512 \times 256$  pixels. The SPAD pixels have a pixel pitch of  $16.4 \mu\text{m}$  and a low fill factor of 10%, owing to the lack of microlenses in the prototype.
- **Prophesee EVK4 event camera**, which is a state-of-the-camera commercial event camera featuring a sensor resolution of  $1280 \times 720$  pixels, pixel pitch of  $4.86 \mu\text{m}$  and a fill-factor of  $> 77\%$ .
- **Photron infinicam** a conventional high-speed camera that can stream acquisition over USB-C at a resolution of  $1246 \times 1024$  pixels and 1 kHz frame-rate. For higher frame rates, it is necessary to reduce the number of rows that are read out—for the example, we use a resolution of  $1246 \times 240$  pixels to obtain acquisition at 4 kHz in Fig. 10.



Supplementary Figure 8: **Cameras and sensor arrays used for the experiments described in Secs. 6.1 and 6.2.** The Infinicam and Prophesee were used for the comparisons made in Figs. 9 and 10 respectively.

### Removing Hot Pixels

A few SPAD pixels (around 5% of the total pixels in our prototype) have extremely high dark current rate and therefore have  $B_t(\mathbf{x}) = 1$  almost always. We detect these *hot pixels* by capturing a photon-cube of 100000 bit-planes in a very dark environment and detecting pixel locations with high photon counts. For video compressive and event imagers, we inpaint projections using OpenCV’s implementation of the Telea algorithm [18]. For motion projections, we do not sum over bit-plane locations that correspond to hot pixels during integration. Further, we remove pixel locations from the hot pixel mask if the motion trajectory provides access to neighboring values that are not hot pixels. We inpaint the motion projection after excluding these points.

### Experiment-wise Lens Specifications

We used C-mount lenses for our experiments with the following focal lengths:

- 12 mm for the comparison to Prophesee EVK4 in Fig. 9. The Prophesee EVK4 and the SwissSPAD2 were used with the same lens specifications.
- 16 mm for the coded exposures shown in Fig. 2.
- 35 mm for the spinning casino roulette shown in Figs. 4 and 10.
- 50 mm for the motion stack shown in Fig. 6 and the traffic scene shown in Fig. 8.
- 75 mm for the falling die sequence shown in Fig. 1, the measure tape sequence shown in Fig. 5, and the water splash captured in Fig. 7.

## 5. UltraPhase Experiments

### Processor Description

The chip consists of a  $3 \times 6$  array of processing cores, each of which can interface with  $4 \times 4$  SPAD pixels via 3D stacking. At this point, the 3D stacking has not been completed, so we interface UltraPhase with the photon-cubes acquired by the SwissSPAD2 [19] instead. Every core is independent, has 4 kb of available RAM, and can execute programs of up to 256 instructions in length at a rate of 140 million instructions per second (MIPS). The system supports a wide range of instructions including, bit-wise operations, 32-bit arithmetic operations, data manipulation and custom inter-core synchronization. For more details, please refer to Ardelean [1].

We implement projections on UltraPhase by using a custom assembly code to program each core separately. We include the commented assembly code for all three projections in Listings 1 to 3. To compute multiple projections, we simply run projections sequentially, one bit-plane at a time. Since each projection can be computed significantly faster than the camera frame rate (e.g., 1.678 ms for video compressive sensing of 40 Hz readout), this does not bottleneck acquisition. We include the processing time for each projection in Tab. 1.

### Measuring Bandwidth

We assume that the outputs for sum, video compressive and motion projections have 12-bit depth. For event cameras, we assume that each event consists of 18-bits—9-bits to encode the pixel location ( $\lceil \log_2(12 \times 24) \rceil$ ), 8 bits to represent the timestamp (corresponding to the bit-plane index where the event was triggered), and 1-bit to encode polarity. We then measure readout on a  $12 \times 24$  region-of-interest (RoI) of the falling die sequence that was acquired using the SwissSPAD2. Table 1 lists the readout bandwidth for each projection.

### Measuring Power

The power consumption of UltraPhase is comprised of compute power and readout power. For compute power, the chip was characterized by executing instructions corresponding to each projection in an infinite loop and measuring its average power consumption. As an upper bound, we assumed the maximum possible power consumption for operations that involved reading and writing to the RAM. This measured power consumption was then scaled by the duty cycle of each projection—which is the ratio of the time required to process a bit-plane to the exposure time of each bit-plane.

For readout power, we consider a conventional digital interface at 3.3 V with a load of 7 pF operating at the specified bandwidth, amounting to 54 nanowatts for each kilobit readout (nW/kbps)—this is similar, for instance, to the USB interface utilized by the SwissSPAD2.

Table 1 provides the processing power, readout power and the total power for each projection. Clearly, processing requires an order of magnitude (or more) lesser power than readout, which explains how computing photon-cube projections results in reduced sensor power consumption.

Table 1: **Power and bandwidth benchmarks** when computing photon-cube projections on UltraPhase, a  $24 \times 12$  array, at 40 Hz readout. We compare computing projections to reading out the entire photon-cube. We report the processing time, the readout bandwidth, and the compute and readout power for each projection.

	Processing time ↓ (ms)	Bandwidth ↓ (kbps)	Power ↓		
			Processing ( $\mu\text{W}$ )	Readout ( $\mu\text{W}$ )	Total ( $\mu\text{W}$ )
12-bit sum image	0.981	135	0.3	7.29	7.6
Snapshot compressive	1.678	135	3.0	7.29	10.3
Motion projection	1.096	135	1.3	7.29	8.6
Event camera	9.817	101.25	2.4	5.83	8.2
Three projections	12.591	405	6.7	21.87	28.6
Photon-cube readout	0.007	28125	$5.4 \times 10^{-3}$	1518.8	1518.8

Table 2: **Power consumption** of SoDaCam versus conventional cameras (in mW), estimated for  $512 \times 256$  pixels at 40 Hz readout. CMOS estimates assume the usage of column-parallel ADCs [15].

	Photon detection		Compute	Readout	Total	
	Dark	Ambient			Dark	Ambient
Photon-cube readout	1	62	-	690	691	752
Sum-image	1	62	0.3	4.5	5.8	66.8
VCS	1	62	1.3	4.5	6.8	67.8
Motion proj.	1	62	0.7	4.5	6.2	67.2
Event camera	1	62	1	3.6	5.6	66.6
Three proj.(s)	1	62	3	13.5	17.5	78.5
CMOS @ 40 FPS	~10–25		-	4.5	~15–30	
CMOS @ 4k FPS	~600–2500		-	450	~1000–3000	

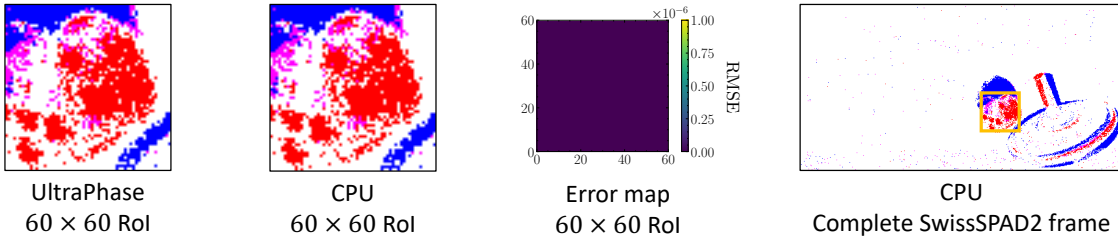
### Comparison to CMOS Sensors

In addition to compute and readout power quantified in the previous section, a computational SPAD also consumes power to detect photons. By incorporating this photon-detection power, we can provide a rough comparison of SoDaCam projections to CMOS sensors. The photon-detection dissipation depends on the number of photon detections, and hence varies with the light level—for the SwissSPAD2, this is measured to be  $< 1\text{mW}$  in the dark and  $\sim 62\text{ mW}$  in indoor lighting [19]. To estimate compute and readout power, we linearly scale the measurements presented in Tab. 1 for an array of  $512 \times 256$  pixels. We note that this is a conservative estimate since UltraPhase is not designed to be a low-power device.

As seen in Tab. 1, under ambient lighting, the power consumption of our emulated cameras is higher than conventional CMOS cameras; while in low light, the SPAD consumes lesser power owing to fewer photon detections. We remark that without the bandwidth reduction facilitated by photon-cube projections, SPADs are at a considerable disadvantage compared to their CMOS counterparts. Finally, we provide a comparison against high-speed CMOS cameras, which can also be used to obtain photon-cube projections, albeit with a read noise penalty (Sec. 6.2), and higher power consumption.

### Visualization of Projections

Since UltraPhase is a low-resolution sensor-processor ( $12 \times 24$  pixels), we visualize projections by repeating computations in a tiled manner to cover a region-of-interest (RoI) of  $60 \times 60$  pixels. Supplementary Figure 9 shows the visualization of an event camera emulated on UltraPhase. To provide more context, we include the CPU visualization of the entire SwissSPAD2 event-frame. We also verified that the outputs of UltraPhase were identical to CPU-run outputs by computing the RMSE between event frames that result from UltraPhase computations and CPU computations (see error map in Supp. Fig. 9).



Supplementary Figure 9: **Event camera computed using UltraPhase**, on 2500 bit-planes of the falling die sequence. For visualization purposes, we run computations on UltraPhase in a tiled manner so as to cover a RoI of  $60 \times 60$  pixels. We compare this to CPU-run outputs of the same RoI and verify that they are identical. For context, we highlight this RoI using a bounding box on the CPU-run event-frame that has a resolution of  $256 \times 512$  pixels. The event simulation parameters used were  $\tau = 0.45, \beta = 0.95, T_0 = 80$ .

**Listing 1: Custom assembly code for implementing video compressive sensing on UltraPhase.** Here, we consider computing one compressive snapshot that is multiplexed by 16 binary random masks.

---

```

--RAM(64..127) stores the 64 subframe compression code masks as one bit per pixel in byte1 and byte0
--The output is available in RAM(0..15)
--CtrlOut is strobed after every binary frame

#define pixelValue 0                --register R0 is used for the pixel values
#define frameIdx 1                  --register R1 is used as a counter for the
  ↳ current binary frame
#define subFrameIdx 2              --register R2 is used as a counter for the current
  ↳ subFrame
#define mask 3                     --register R3 is used to store the
  ↳ compression codes for the current subframe
#define aux0 4                     --register R4 is used for
#define aux1 5                     --register R5 is used for
#define CtrlOut 0b10000            --address for external trigger signal
#define toMask 0b001000           --address used to fetch to R3 (mask)

0: LOAD subFrameIdx, $64, 0        --initialize subFrame pointer to 0 + 64 (RAM offset)
1: LOAD subFrameIdx, $0, 1
2: LOAD frameIdx, $16, 0          --initialize frameIdx pointer to 16 i.e. number of
  ↳ bit_planes_per_subframe
3: LOAD frameIdx, $0, 1

4: GETP 5, 1, 0                  --get pixel data and store it in R0
  ↳ (pixelValue)
5: FETCH @subFrameIdx, toMask, 0  --get the appropriate mask
6: AND pixelValue, mask, pixelValue --apply mask i.e. multiply with code[subframe]
7: CALL 50                       --accumulate pixels
8: TELL CtrlOut, 0               --strobe CtrlOut

-----
-- update indexes
9: OR aux0, aux0, aux0           --clear flags
10: SUBC frameIdx, $1            --decrement frameIdx
11: JUMPZ 13                     --check if we finished with all the binary
  ↳ planes per subframe
12: JUMP 4                       --if not, then move on
13: OR aux0, aux0, aux0          --clear flags
14: ADDC subFrameIdx, $1         --move to next subFrame
15: JUMP 2                       --reset frameIdx and continue

-----
-- this subroutine will accumulate the pixel values from pixelValue
50: LOAD aux0, $16, 0            --set R4 (aux0) to 16
51: LOAD aux0, $0, 1
52: LOAD aux1, $0, 0             --set R5 (aux1) to 0
53: LOAD aux1, $0, 1
54: OR aux0, aux0, aux0          --clear flags
55: SR0 pixelValue, pixelValue   --extract one pixel
56: ADDC (aux0), aux1, (aux0)    --increment if pixel is 1
57: SUBC aux0, $1                --decrement counter
58: JUMPNZ 54                   --repeat until done with all 16 pixels
59: RET

```

---

Listing 2: Custom assembly code for implementing event cameras on UltraPhase.

```

--The core will strobe CtrlOut every time an event took place and the SoC needs to read RAM(0) to get it

#define toaux0 0b000010
#define toaux1 0b000100
#define pixelValue 0          --register R0 is used for the binary pixel values
#define aux0 1                --register R1 is used for misc
#define aux1 2                --register R2 is used for misc
#define Bpointer 3           --register R3 is used as a pointer to the reference_average stored in
    ↪ RAM(17..32)
#define Apointer 4           --register R4 is used as a pointer to the current_average stored in
    ↪ RAM(1..16)
#define pixelIdx 5           --register R5 is used for the current pixel index
#define CtrlOut 0b10000      --address for external trigger signal
#define NOut 0b01000         --address for north trigger signal
#define decayAddress 127     --RAM address 127 stores the exponential_decay
#define decayComplementAddress 126 --RAM address 126 stores the value for 1-exponential_decay
#define intervalAddress 125  --RAM address 125 stores the initial_interval
#define thresholdAddress 124 --RAM address 124 stores the contrast_threshold
#define frameIdxAddress 123  --RAM address 123 stores the frame_index counter

0: GETP 5, 1, 0                --get pixel data and
    ↪ store it in R0 (pixelValue)
1: LOAD pixelIdx, $0, 1       --set R5 (pixelIdx) to
    ↪ 16 to use as counter for the pixels
2: LOAD pixelIdx, $16, 0
3: LOAD Apointer, $0, 1       --initialize pointers
4: LOAD Apointer, $1, 0
5: LOAD Bpointer, $0, 1
6: LOAD Bpointer, $17, 0

7: FETCH @decayAddress, toaux0, 0 --get decay constant from RAM and
    ↪ store it into R1 (aux0)
8: FETCH @decayComplementAddress, toaux1, 0 --get (1 - decay) constant from RAM and
    ↪ store it into R2 (aux1)

9: MUL (Apointer), aux0, (Apointer) -- current_average[pixelIdx]
    ↪ exponential_decay * current_average[pixelIdx]
10: SRX (Apointer), (Apointer) -- 8 fractional bit
    ↪ multiplication
11: SRX (Apointer), (Apointer)
12: SRX (Apointer), (Apointer)
13: SRX (Apointer), (Apointer)
14: SRX (Apointer), (Apointer)
15: SRX (Apointer), (Apointer)
16: SRX (Apointer), (Apointer)
17: SRX (Apointer), (Apointer)

18: SR0 pixelValue, pixelValue --shift R0 (pixelValue) to the
    ↪ right and pad with 0; the pixel bit is loaded into the carry flag
19: JUMPNC 21                  --current_average[pixelIdx]
    ↪
    ↪ current_average[pixelIdx] + (1-exponential_decay) * 0
20: ADD (Apointer), aux1, (Apointer) --current_average[pixelIdx]
    ↪ current_average[pixelIdx] + (1-exponential_decay) * 1
21: FETCH @frameIdxAddress, toaux0, 0 --get frame_index from RAM and store it into
    ↪ R1 (aux0)
22: FETCH @intervalAddress, toaux1, 0 --get initial_interval from RAM and store it
    ↪ into R2 (aux1)
23: CMP aux0, aux1            --check if
    ↪ frame_index < initial_interval
24: JUMPNC 40                  --if not, jump and
    ↪ process

```

```

25: FETCH (Apointer), toaux0, 0                --if yes, get
   ↳ current_average[pixelIdx]
26: STORE aux0, (Bpointer)                    --reference_average[pixelIdx]
   ↳ current_average[pixelIdx]
27: JUMP 70                                    --GO TO NEXT
   ↳ PIXEL

-- frame_index is larger than initial_interval
40: FETCH (Apointer), toaux0, 0                --if not, get
   ↳ current_average[pixelIdx] and store it into R1 (aux0)
41: FETCH (Bpointer), toaux1, 0                --get
   ↳ reference_average[pixelIdx] and store it into R2 (aux1)
42: SUB aux0, aux1, aux0                       --diff[pixelIdx]
   ↳ current_average[pixelIdx] - reference_average[pixelIdx] and store it into R1 (aux0)
43: JUMPNC 60                                  --diff is
   ↳ positive

-- compare abs(diff) with threshold if diff is negative
44: FETCH @thresholdAddress, toaux1, 0         --get contrast_threshold and store it
   ↳ into R2 (aux1)
45: NEG aux1, aux1                             --diff is negative,
   ↳ so make contrast_threshold negative and store it into R2 (aux1)
46: CMP aux0, aux1                             --if diff <
   ↳ -contrast_threshold
47: JUMPNC 70                                  --if not, GO TO
   ↳ NEXT PIXEL
48: NEG pixelIdx, @0                            --RAM(0) pixel_index
   ↳ i.e. a negative event
49: ADD (Bpointer), aux1, (Bpointer)           --reference_average + contrast_threshold *
   ↳ (-1)
50: TELL CtrlOut, 0                            --strobe CtrlOut to
   ↳ signal an event
51: JUMP 70                                    --GO TO NEXT
   ↳ PIXEL

-- compare abs(diff) with threshold if diff is positive
60: FETCH @thresholdAddress, toaux1, 0         --get contrast_threshold and store it
   ↳ into R2 (aux1)
61: CMP aux1, aux0                             --if diff >
   ↳ contrast_threshold
62: JUMPNC 70                                  --if not, GO TO
   ↳ NEXT PIXEL
63: STORE pixelIdx, @0                         --RAM(0) pixel_index
   ↳ i.e. a positive event
64: ADD (Bpointer), aux1, (Bpointer)           --reference_average + contrast_threshold *
   ↳ 1
65: TELL CtrlOut, 0                            --strobe CtrlOut to
   ↳ signal an event
66: JUMP 70                                    --GO TO NEXT
   ↳ PIXEL

--GO TO NEXT PIXEL
70: OR pixelValue, pixelValue, pixelValue     --clear flags
71: ADDC Apointer, $1                          --increment Apointer
72: ADDC Bpointer, $1                          --increment Bpointer
73: SUBC pixelIdx, $1                          --decrement pixel counter
74: JUMPNZ 7                                   --if not done with
   ↳ pixels, go to next one
75: FETCH @frameIdxAddress, toaux0, 0         --if done with pixels, increment frame
   ↳ counter and get new pixel values
76: TELL NOut, 0                               --strobe NOut to signal
   ↳ a new exposure
77: ADDC aux0, $1
78: STORE aux0, @frameIdxAddress
79: JUMP 0

```

---

Listing 3: Custom assembly code for implementing motion projections on UltraPhase. Without loss of generality, we consider a linear projection along the horizontal direction.

```

--The projection is available in RAM(0..15)
-- CtrlOut is strobed after every frame

#define Xshift 0          --register R0 is used for the horizontal shift
#define timestep 1       --register R1 is used for the current timestep
#define origPixels 2     --register R2 is used for the current core's pixels
#define shiftPixels 3    --register R3 is used for the shifted pixels
#define aux0 4           --register R4 is used for misc
#define aux1 5           --register R5 is used for misc
#define CtrlOut 0b10000 --address for external trigger signal
#define shiftL3neighAddr 127 --RAM(127) stores the 0b0111_0111_0111_0111 mask
#define shiftL3currAddr 126 --RAM(126) stores the 0b1000_1000_1000_1000 mask
#define shiftL2neighAddr 125 --RAM(125) stores the 0b0011_0011_0011_0011 mask
#define shiftL2currAddr 124 --RAM(124) stores the 0b1100_1100_1100_1100 mask
#define shiftL1neighAddr 123 --RAM(123) stores the 0b0001_0001_0001_0001 mask
#define shiftL1currAddr 122 --RAM(122) stores the 0b1110_1110_1110_1110 mask

0: LOAD Xshift, $0xFFF8, 0          --load -8 into Xshift as initial value
1: LOAD Xshift, $0xFFFF, 1
2: CALL 50                        --get the correct pixel values according to Xshift
3: CALL 30                        --accumulate pixels
4: CALL 20                        --advance time
5: TELL CtrlOut, 0                -- strobe CtrlOut to signal a new frame
6: JUMP 2                          --repeat

-----
-- this subroutine will advance timestep and update Xshift
20: OR timestep, timestep, timestep --clear flags
21: ADDC timestep, $1              --increment timestep
22: OR timestep, timestep, aux0    --copy timestep to aux0
23: SPLIT aux0, 5, 0b010000       --timestep / timestep/1024
24: SR0 aux0, aux0
25: SR0 aux0, aux0
26: LOAD aux1, $1, 0              --load aux1 with the Xspeed value of 1
27: MAC aux0, aux1, Xshift, Xshift --Xshift += Xspeed*timestep/2
28: RET

-----
-- this subroutine will accumulate the pixel values from shiftPixels
30: LOAD aux0, $16, 0             --set R4 (aux0) to 16
31: LOAD aux0, $0, 1
32: LOAD aux1, $0, 0              --set R5 (aux1) to 0
33: LOAD aux1, $0, 1
34: OR aux0, aux0, aux0           --clear flags
35: SR0 shiftPixels, shiftPixels  --extract one pixel
36: ADDC (aux0), aux1, (aux0)     --increment if pixel is 1
37: SUBC aux0, $1                 --decrement counter
38: JUMPNZ 34                      --repeat until done with all 16 pixels
39: RET

-----
-- this subroutine will get pixel values from the core and the correct neighbour based on the Xshift
50: GETP 5, 4, 0                  --get pixel values and store them in R2
   ← (origPixels)
51: OR Xshift, Xshift, aux1        --copy current shift into R5 (aux1)
52: LOAD aux0, $0, 0              --set R4 (aux0) to 0 to use for Xshift comparison
53: LOAD aux0, $0, 1
54: CMP aux1, aux0                --compare current shift with 0
55: JUMPZ 115                      --current shift = 0
56: JUMPC 120                      --current shift < 0
57: JUMP 58                        --current shift > 0

-----
-- positive shifts

```

```

58: LOAD aux0, $4, 0          --set R4 (aux0) to 4 for current shift comparison
59: LOAD aux0, $0, 1
60: CMP aux0, aux1
61: JUMPC 105                  --current shift > 4, read from the neighbour's neighbour
62: JUMPZ 100                  --current shift is 4
63: LOAD aux0, $2, 0          --set R4 (aux0) to 2, for current shift comparison
64: CMP aux0, aux1
65: JUMPC 90                   --current shift is 3
66: JUMPZ 80                   --current shift is 2

-- shift is 1
67: SL0 shiftPixels, shiftPixels --pixels from the neighbour need to be shifted
   ↳ to the left 3 times
68: SL0 shiftPixels, shiftPixels
69: SL0 shiftPixels, shiftPixels
70: OR origPixels, origPixels, aux1 --save curent pixels in the aux1 variable
71: SR0 aux1, aux1            --pixels from this core need
   ↳ to be shifted to the right once
72: AND shiftPixels, @shiftL3currAddr, shiftPixels --apply mask to select relevant bits from
   ↳ neighbour
73: AND aux1, @shiftL3neighAddr, aux1 --apply mask to select relevant bits from
   ↳ current core
74: OR shiftPixels, aux1, shiftPixels --combine to create final pixel values
75: RET

-- shift is 2
80: SL0 shiftPixels, shiftPixels --pixels from neighbour need to
   ↳ be shifted to the left 2 times
81: SL0 shiftPixels, shiftPixels
82: OR origPixels, origPixels, aux1 --save curent pixels in the aux1
   ↳ variable
83: SR0 aux1, aux1            --pixels from
   ↳ this core need to be shifted to the right 2 times
84: SR0 aux1, aux1
85: AND shiftPixels, @shiftL2currAddr, shiftPixels --apply mask to select relevant bits from
   ↳ neighbour
86: AND aux1, @shiftL2neighAddr, aux1 --apply mask to select relevant
   ↳ bits from current core
87: OR shiftPixels, aux1, shiftPixels --combine to create final pixel
   ↳ values
88: RET

-- shift is 3
90: SL0 shiftPixels, shiftPixels --pixels from neighbour need to
   ↳ be shifted to the left once
91: OR origPixels, origPixels, aux1 --save curent pixels in the aux1
   ↳ variable
92: SR0 aux1, aux1            --pixels from
   ↳ this core need to be shifted to the right 3 times
93: SR0 aux1, aux1
94: SR0 aux1, aux1
95: AND shiftPixels, @shiftL1currAddr, shiftPixels --apply mask to select relevant bits from
   ↳ neighbour
96: AND aux1, @shiftL1neighAddr, aux1 --apply mask to select relevant
   ↳ bits from current core
97: OR shiftPixels, aux1, shiftPixels --combine to create final pixel
   ↳ values
98: RET

-- shift is 4
100: PUTN origPixels, 4        --shift your pixels to the left (share pixels with
   ↳ neighbour)
101: SAVEN 1                  --save pixels from righth neighbour
102: GETN 0, 8, 0            --get pixels from righth neighbour and store in
   ↳ shiftPixels
103: RET

```

```

-- shift is > 4
105: PUTN origPixels, 4          --shift your pixels to the left (share pixels with
   ↳ neighbour)
106: SAVEN 1                    --save pixels from right neighbour
107: GETN 0, 8, 0              --get pixels from right neighbour and store in
   ↳ shiftPixels
108: OR aux1, aux1, aux1       --clear Carry flag
109: SUBC aux1, $4             --subtract 4 from current shift because we read from
   ↳ a neighbour
110: JUMP 58

```

```

-----
-- shift is zero
115: OR origPixels, origPixels, shiftPixels --the shift is zero, so keep the pixels
116: RET

```

```

-----
-- negative shifts
120: LOAD aux0, $FFFC, 0       --set R4 (aux0) to -4 to use for current shift comparison
121: LOAD aux0, $0xFFFF, 1
122: CMP aux1, aux0
123: JUMPC 170                 --current shift < -4 so we need to read from
   ↳ neighbour's neighbour
124: JUMPZ 160                 --current shift is -4
125: LOAD aux0, $FFFE, 0       --set R4 (aux0) to -2 to use for current shift comparison
126: CMP aux1, aux0
127: JUMPC 150                 --current shift is -3
128: JUMPZ 140                 --current shift is -2

```

```

-- shift is -1
129: SR0 shiftPixels, shiftPixels --pixels from
   ↳ neighbour need to be shifted to the right 3 times
130: SR0 shiftPixels, shiftPixels
131: SR0 shiftPixels, shiftPixels
132: OR origPixels, origPixels, aux1 --save curent pixels in
   ↳ the aux1 variable
133: SL0 aux1,                  --pixels from
   ↳ aux1
   ↳ this core need to be shifted to the left once
134: AND shiftPixels, @shiftL1neighAddr, shiftPixels --apply mask to select relevant bits from
   ↳ neighbour
135: AND aux1, @shiftL1currAddr, aux1 --apply mask to select
   ↳ relevant bits from current core
136: OR shiftPixels, aux1, shiftPixels --combine to create final
   ↳ pixel values
137: RET

```

```

-- shift is -2
140: SR0 shiftPixels, shiftPixels --pixels from
   ↳ neighbour need to be shifted to the right 2 times
141: SR0 shiftPixels, shiftPixels
142: OR origPixels, origPixels, aux1 --save curent pixels in
   ↳ the aux1 variable
143: SL0 aux1,                  --pixels from
   ↳ aux1
   ↳ this core need to be shifted to the left 2 times
144: SL0 aux1, aux1
145: AND shiftPixels, @shiftL2neighAddr, shiftPixels --apply mask to select relevant bits from
   ↳ neighbour
146: AND aux1, @shiftL2currAddr, aux1 --apply mask to select
   ↳ relevant bits from current core
147: OR shiftPixels, aux1, shiftPixels --combine to create final
   ↳ pixel values
148: RET

```

```

-- shift is -3

```

```

150: SR0 shiftPixels, shiftPixels           --pixels from
↪ neighbour need to be shifted to the right once
151: OR origPixels, origPixels, aux1       --save curent pixels in
↪ the aux1 variable
152: SL0 aux1,                             --pixels from
↪ aux1
↪ this core need to be shifted to the left 3 times
153: SL0 aux1, aux1
154: SL0 aux1, aux1
155: AND shiftPixels, @shiftL3neighAddr, shiftPixels --apply mask to select relevant bits from
↪ neighbour
156: AND aux1, @shiftL3currAddr, aux1      --apply mask to select
↪ relevant bits from current core
157: OR shiftPixels, aux1, shiftPixels     --combine to create final
↪ pixel values
158: RET

-- shift is -4
160: PUTN origPixels, 1                   --shift your pixels to the right (share pixels with
↪ neighbour)
161: SAVEN 4                             --save pixels from left neighbour
162: GETN 2, 8, 0                         --get pixels from left neighbour and store in
↪ shiftPixels
163: RET

-- shift is < -4
170: PUTN origPixels, 1                   --shift your pixels to the right (share pixels with
↪ neighbour)
171: SAVEN 4                             --save pixels from left neighbour
172: GETN 2, 8, 0                         --get pixels from left neighbour and store in
↪ shiftPixels
173: OR aux1, aux1, aux1                  --clear Carry flag
174: ADDC aux1, $4                         --add 4 to current shift because we read from a
↪ neighbour
175: JUMP 120

```

---

## Supplementary References

- [1] A. Ardelean. *Computational Imaging SPAD Cameras*. PhD thesis, École polytechnique fédérale de Lausanne, 2023.
- [2] S. Baker, D. Scharstein, J. Lewis, S. Roth, M. J. Black, and R. Szeliski. A database and evaluation methodology for optical flow. *International journal of computer vision*, 92:1–31, 2011.
- [3] C. Brandli, R. Berner, M. Yang, S.-C. Liu, and T. Delbruck. A  $240 \times 180$  130 dB 3  $\mu$ s latency global shutter spatiotemporal vision sensor. *IEEE Journal of Solid-State Circuits*, 49(10):2333–2341, 2014. doi: 10.1109/JSSC.2014.2342715.
- [4] J. E. Bresenham. Algorithm for computer control of a digital plotter. *IBM Systems journal*, 4(1):25–30, 1965.
- [5] S. H. Chan, X. Wang, and O. A. Elgendy. Plug-and-play admm for image restoration: Fixed-point convergence and applications. *IEEE Transactions on Computational Imaging*, 3(1):84–98, 2017. doi: 10.1109/TCI.2016.2629286.
- [6] S. Chen and M. Guo. Live demonstration: Celex-v: A 1m pixel multi-mode event-based sensor. In *Proceedings of the IEEE/CVF Conference on Computer Vision and Pattern Recognition (CVPR) Workshops*, June 2019.
- [7] X. Y. Chengshuai Yang, Shiyu Zhang. Ensemble learning priors driven deep unfolding for scalable video snapshot compressive imaging. In *IEEE European Conference on Computer Vision (ECCV)*, 2022.
- [8] G. Gallego, H. Rebecq, and D. Scaramuzza. A unifying contrast maximization framework for event cameras, with applications to motion, depth, and optical flow estimation. In *Proceedings of the IEEE Conference on Computer Vision and Pattern Recognition (CVPR)*, June 2018.
- [9] Y. Li, M. Qi, R. Gulve, M. Wei, R. Genov, K. N. Kutulakos, and W. Heidrich. End-to-end video compressive sensing using anderson-accelerated unrolled networks. In *2020 IEEE International Conference on Computational Photography (ICCP)*, pages 1–12, 2020. doi: 10.1109/ICCP48838.2020.9105237.
- [10] Y. Liu, X. Yuan, J. Suo, D. J. Brady, and Q. Dai. Rank minimization for snapshot compressive imaging. *IEEE Trans. Pattern Anal. Mach. Intell.*, 41(12):2990 – 3006, 2019. doi: 10.1109/TPAMI.2018.2873587. URL <https://doi.org/10.1109/TPAMI.2018.2873587>.
- [11] S. Ma, S. Gupta, A. C. Ulku, C. Bruschini, E. Charbon, and M. Gupta. Quanta burst photography. *ACM Transactions on Graphics*, 39(4):1–16, July 2020. ISSN 0730-0301, 1557-7368.
- [12] A. I. Maqueda, A. Loquercio, G. Gallego, N. García, and D. Scaramuzza. Event-based vision meets deep learning on steering prediction for self-driving cars. In *Proceedings of the IEEE Conference on Computer Vision and Pattern Recognition (CVPR)*, June 2018.
- [13] H. Rebecq, R. Ranftl, V. Koltun, and D. Scaramuzza. Events-to-video: Bringing modern computer vision to event cameras. In *Proceedings of the IEEE/CVF Conference on Computer Vision and Pattern Recognition (CVPR)*, June 2019.
- [14] P. Shedligeri, A. S, and K. Mitra. A unified framework for compressive video recovery from coded exposure techniques. In *Proceedings of the IEEE/CVF Winter Conference on Applications of Computer Vision (WACV)*, pages 1600–1609, January 2021.
- [15] M. F. Snoeij, A. J. P. Theuwissen, K. A. A. Makinwa, and J. H. Huijsing. Multiple-Ramp Column-Parallel ADC Architectures for CMOS Image Sensors. *IEEE JSSC*, 2007. doi: 10.1109/JSSC.2007.908720.
- [16] M. Tassano, J. Delon, and T. Veit. Fastdvdnet: Towards real-time deep video denoising without flow estimation. In *Proceedings of the IEEE/CVF Conference on Computer Vision and Pattern Recognition (CVPR)*, June 2020.
- [17] Z. Teed and J. Deng. Raft: Recurrent all-pairs field transforms for optical flow. In *European Conference on Computer Vision*, 2020.
- [18] A. Telea. An image inpainting technique based on the fast marching method. *Journal of graphics tools*, 9(1):23–34, 2004.
- [19] A. C. Ulku, C. Bruschini, I. M. Antolovic, Y. Kuo, R. Ankri, S. Weiss, X. Michalet, and E. Charbon. A  $512 \times 512$  SPAD Image Sensor With Integrated Gating for Widefield FLIM. *IEEE Journal of Selected Topics in Quantum Electronics*, 25(1):1–12, Jan. 2019. ISSN 1077-260X, 1558-4542. doi: 10.1109/JSTQE.2018.2867439.
- [20] S. V. Venkatakrishnan, C. A. Bouman, and B. Wohlberg. Plug-and-play priors for model based reconstruction. In *2013 IEEE Global Conference on Signal and Information Processing*, pages 945–948, 2013. doi: 10.1109/GlobalSIP.2013.6737048.
- [21] Z. Wan, Y. Dai, and Y. Mao. Learning dense and continuous optical flow from an event camera. *IEEE Transactions on Image Processing*, 31:7237–7251, 2022. doi: 10.1109/TIP.2022.3220938.

- [22] Z. Wang, H. Zhang, Z. Cheng, B. Chen, and X. Yuan. Metasci: Scalable and adaptive reconstruction for video compressive sensing. In *Proceedings of the IEEE/CVF Conference on Computer Vision and Pattern Recognition (CVPR)*, pages 2083–2092, June 2021.
- [23] Z. Wu, J. Zhang, and C. Mou. Dense deep unfolding network with 3D-CNN prior for snapshot compressive imaging. In *Proceedings of the IEEE/CVF International Conference on Computer Vision (ICCV)*, pages 4892–4901, October 2021.
- [24] X. Yuan. Generalized alternating projection based total variation minimization for compressive sensing. In *2016 IEEE International Conference on Image Processing (ICIP)*, pages 2539–2543, 2016. doi: 10.1109/ICIP.2016.7532817.
- [25] X. Yuan, D. J. Brady, and A. K. Katsaggelos. Snapshot compressive imaging: Theory, algorithms, and applications. *IEEE Signal Processing Magazine*, 38(2):65–88, 2021.
- [26] X. Yuan, Y. Liu, J. Suo, F. Durand, and Q. Dai. Plug-and-play algorithms for video snapshot compressive imaging. *IEEE Transactions on Pattern Analysis and Machine Intelligence*, 44(10):7093–7111, 2022. doi: 10.1109/TPAMI.2021.3099035.
- [27] A. Z. Zhu, L. Yuan, K. Chaney, and K. Daniilidis. Unsupervised event-based learning of optical flow, depth, and egomotion. In *Proceedings of the IEEE/CVF Conference on Computer Vision and Pattern Recognition*, pages 989–997, 2019.